

1 **Integrating faults and past earthquakes into a probabilistic seismic hazard**
2 **model for peninsular Italy**

3

4 Alessandro Valentini¹, Francesco Visini² and Bruno Pace¹

5 ¹ DiSPUTer, Università degli Studi “Gabriele d’Annunzio”, Chieti, Italy

6 ² Istituto Nazionale di Geofisica e Vulcanologia, L’Aquila, Italy

7

8 **Abstract**

9

10 *Italy is one of the most seismically active countries in Europe. Moderate to strong earthquakes, with*
11 *magnitudes of up to ~7, have been historically recorded for many active faults. Currently,*
12 *probabilistic seismic hazard assessments in Italy are mainly based on area source models, in which*
13 *seismicity is modelled using a number of seismotectonic zones and the occurrence of earthquakes is*
14 *assumed uniform. However, in the past decade, efforts have increasingly been directed towards using*
15 *fault sources in seismic hazard models to obtain more detailed and potentially more realistic patterns*
16 *of ground motion. In our model, we used two categories of earthquake sources. The first involves*
17 *active faults, and geological slip rates were used to quantify the seismic activity rate. We produced an*
18 *inventory of all fault sources with details of their geometric, kinematic and energetic properties. The*
19 *associated parameters were used to compute the total seismic moment rate of each fault. We*
20 *evaluated the magnitude-frequency distribution (MFD) of each fault source using two models: a*
21 *characteristic Gaussian model centred at the maximum magnitude and a Truncated Gutenberg-*
22 *Richter model. The second earthquake source category involves grid-point seismicity, with a fixed-*
23 *radius smoothed approach and a historical catalogue were used to evaluate seismic activity. Under*
24 *the assumption that deformation is concentrated along faults, we combined the MFD derived from the*
25 *geometry and slip rates of active faults with the MFD from the spatially smoothed earthquake sources*
26 *and assumed that the smoothed seismic activity in the vicinity of an active fault gradually decreases*
27 *by a fault size-driven factor. Additionally, we computed horizontal peak ground acceleration maps for*
28 *return periods of 475 and 2,475 yrs. Although the ranges and gross spatial distributions of the*
29 *expected accelerations obtained here are comparable to those obtained through methods involving*
30 *seismic catalogues and classical zonation models, the spatial pattern of the hazard maps obtained*
31 *with our model is far more detailed. Our model is characterized by areas that are more hazardous*
32 *and that correspond to mapped active faults, while previous models yield expected accelerations that*
33 *are almost uniformly distributed across large regions. In addition, we conducted sensitivity tests to*

34 *determine the impact on the hazard results of the earthquake rates derived from two MFD models for*
35 *faults and to determine the relative contributions of faults versus distributed seismic activity. We*
36 *believe that our model represents advancements in terms of the input data (quantity and quality) and*
37 *methodology used in the field of fault-based regional seismic hazard modelling in Italy.*
38

39 **1. Introduction**

40 In this paper, we present the results of an alternative seismogenic source model for
41 use in a probabilistic seismic hazard assessment (PSHA) for Italy that integrates
42 active fault and seismological data. The use of active faults as an input for seismic
43 hazard analysis is a consolidated approach in many countries characterized by high
44 strain rates and seismic releases, as shown, for example, by Field et al. (2015) in
45 California and Stirling et al. (2012) in New Zealand. Moreover, in recent years, active
46 fault data have also been successfully integrated into seismic hazard studies or
47 models, in regions with moderate-to-low strain rates, such as SE Spain (e.g., Garcia-
48 Mayordomo et al., 2007), France (e.g., Scotti et al., 2014), and central Italy (e.g.,
49 Peruzza et al., 2011).

50 In Europe, a working group of the European Seismological Commission, named
51 *Fault2SHA*, is discussing fault-based seismic hazard modelling
52 (<https://sites.google.com/site/linkingfaultpsa/home>). The working group, born to
53 motivate exchanges between field geologists, fault modellers and seismic hazard
54 practitioners, and it is a community initiative with long term vision on studying the
55 active faults. The work we are presenting here stems from the activities of the
56 *Fault2SHA* working group.

57 Combining active faults and background sources is one of the key aspects in this
58 type of approach. Although the methodology remains far from identifying a standard
59 procedure, common approaches combine active faults and background sources by
60 applying a threshold magnitude, generally between 5.5 and 7, above which
61 seismicity is modelled as occurring on faults and below which seismicity is modelled
62 via a smoothed approach (e.g., Akinci et al., 2009; Danciu et al., 2017), area sources
63 (e.g., the so-called FSBG model in the 2013 European Seismic Hazard Model,
64 ESHM13; Woessner et al., 2015) or a combination of the two (Field et al., 2015;
65 Pace et al., 2006).

66 Another important aspect in the use of active faults to build a seismogenic source
67 model is the use of an appropriate MFD to characterize the temporal model
68 describing the seismic activity of faults. Gutenberg-Richter (GR) and characteristic
69 earthquake models are commonly used, and the choice sometimes depends on the
70 knowledge of the fault and data availability. Often, the choice of the “appropriate”
71 MFD for each fault source is a difficult task because palaeoseismological studies are
72 scarce, and it is often difficult to establish clear relationships between mapped faults
73 and historical seismicity. Recently, Field et al. (2017) discussed the effects and
74 complexity of the choice, highlighting how often the GR model results are not
75 consistent with data; however, in other cases, uncharacteristic behaviour, with rates
76 smaller than the maximum, are possible. The discussion is open (see for example
77 the discussion by Kagan et al., 2012) and far from being solved with the available
78 observations, including both seismological and/or geological/paleoseismological
79 observations. In this work, we explore the calculations of these two MFD, a
80 characteristic Gaussian model and a Truncated Gutenberg-Richter model, to explore
81 the epistemic uncertainties and to consider a *Mixed model* as a so-called “expert
82 judgment” model. This *Mixed model* approach, in which we assigned one of the two
83 MFDs to each fault source, is useful for comparison analysis. The rationale of the
84 choice of the MFD of each fault source is explained in detail later in this paper.
85 However, this approach obviously does not solve this issue, that can be treated as
86 epistemic uncertainties using logic tree or random sampling but, in any case, the
87 choice of MFD remains an open question in fault-based PSHA.

88 In Italy, the current national PSH model for building code (Stucchi et al., 2011) is
89 based on area sources and the classical Cornell approach (Cornell, 1968), in which
90 the occurrence of earthquakes is assumed uniform in the defined seismotectonic
91 zones. However, we believe that more efforts must be directed towards using
92 geological data (e.g., fault sources and paleoseismological information) in PSHA to
93 use slip-rates that describe longer seismic cycles to match the larger magnitudes,
94 extend the observational time required to capture the recurrence of large-magnitude
95 events and therefore improve the reliability of seismic hazard assessments. In fact,
96 as highlighted by the 2016-2017 seismic sequences in central Italy, a zone-based
97 source model is not able to model local spatial variations in ground motion (Meletti et
98 al., 2016), whereas a fault-based model can provide insights for aftershock time-

99 dependent hazard analysis (Peruzza et al., 2016). In conclusion, even if the main
100 purpose of this work is to integrate active faults into hazard calculations for the Italian
101 territory, this study does not represent an official update of the seismic hazard model
102 of Italy.

103

104 **2. Source Inputs**

105 Two earthquake-source inputs are considered in this work. The first is a fault source
106 input that is based on active faults and uses the geometries and slip rates of known
107 active faults to compute activity rates over a certain range of magnitudes. The
108 second is a classical smoothed approach that accounts for the rates of expected
109 earthquakes with a minimum moment magnitude (M_w) of 4.5 but excludes
110 earthquakes associated with known faults based on a modified earthquake
111 catalogue. Note that our seismogenic source requires the combination of the two
112 source inputs related to the locations of expected seismicity rates into a single
113 source model. Therefore, these two earthquake-source inputs are not independent
114 but complementary, in both the magnitude and frequency distribution, and together
115 account for spatial and temporal distribution of the seismicity in Italy.

116 In the following subsections, we describe the two source inputs and how they are
117 combined in the seismogenic source model.

118 **2.1 Fault Source Input**

119 In seismic hazard assessment, an active fault is a structure that exhibits evidence of
120 activity in the late Quaternary, has a demonstrable or potential capability of
121 generating major earthquakes and is capable of future reactivation (e.g. Machette,
122 2000, Danciu et al., 2017). The evidence of Quaternary activity can be
123 geomorphological and/or paleoseismological when activation information from
124 instrumental seismic sequences and/or association to historical earthquakes is not
125 available. Fault source data and location are useful for seismic hazard studies, and
126 we compiled a database for Italy via the analysis and synthesis of neotectonic and
127 seismotectonic data from approximately 90 published studies of 110 faults across
128 Italy. Our database included, but was not limited to, the Database of Individual
129 Seismogenic Sources (DISS vers. 3.2.0, <http://diss.rm.ingv.it/diss/>), which is already

130 available for Italy. It is important to highlight that the DISS is currently composed of
131 two main categories of seismogenic sources: individual and composite sources. The
132 latter are defined by the DISS' authors as "*simplified and three-dimensional*
133 *representation of a crustal fault containing an unspecified number of seismogenic*
134 *sources that cannot be singled out. Composite seismogenic sources are not*
135 *associated with a specific set of earthquakes or earthquake distribution", and*
136 therefore are not useful for our PSHA approach; the former is "*a simplified and three-*
137 *dimensional representation of a rectangular fault plane. Individual seismogenic*
138 *sources are assumed to exhibit characteristic behaviour with respect to rupture*
139 *length/width and expected magnitude"* ([http://diss.rm.ingv.it/diss/index.php/about/13-](http://diss.rm.ingv.it/diss/index.php/about/13-introduction)
140 [introduction](http://diss.rm.ingv.it/diss/index.php/about/13-introduction)). Even if in agreement with our approach, we note that some of the
141 individual seismogenic sources in the DISS are based on geological and
142 paleoseismological information, and many others used the *Boxer* code (Gasperini et
143 al., 1999) to calculate the epicentre, moment magnitude, size and orientation of a
144 seismic source from observed macroseismic intensities. We carefully analysed the
145 individual sources and some related issues: (i) the lack of updating of the geological
146 information of some individual sources and (ii) the nonconformity between the input
147 data used by DISS in *Boxer* and the latest historical seismicity (CPTI15) and
148 macroseismic intensity (DBMI15) publications. Thus, we performed a full review of
149 the fault database. We then compiled a fault source database as a synthesis of
150 works published over the past twenty years, including DISS, using all updated and
151 available geological, paleoseismological and seismological data (see the
152 supplemental files for a complete list of references). We consider our database as
153 complete as possible in terms of individual seismogenic sources, and it contains all
154 the parameters necessary to construct an input dataset for fault-based PSHA.

155 The resulting database of normal and strike-slip active and seismogenic faults in
156 peninsular Italy (Fig. 1, Tables 1 and 2; see the supplemental files) includes all the
157 available geometric, kinematic, slip rate and earthquake source-related information.
158 In the case of missing data regarding the geometric parameters of dip and rake, we
159 assumed typical dip and rake values of 60° and -90°, respectively, for normal faults
160 and 90° and 0° or 180°, respectively, for strike-slip faults. In this paper, only normal
161 and strike-slip faults are used as fault source inputs. We decided not to include thrust
162 faults in the present study because, with the methodology proposed in this study (as

163 discussed later in the text), the maximum size of a single-rupture segment must be
164 defined, and segmentation criteria have not been established for large thrust zones.
165 Moreover, our method uses long-term geological slip rates to derive active seismicity
166 rates, and sufficient knowledge of these values is not available for thrust faults in
167 Italy. Because some areas of Italy, such as the NW sector of the Alps, Po Valley, the
168 offshore sector of the central Adriatic Sea, and SW Sicily, may be excluded by this
169 limitation, we are considering an update to our approach to include thrust faults and
170 volcanic sources in a future study. The upper and lower boundaries of the
171 seismogenic layer are mainly derived from the analysis of Stucchi et al. (2011) of the
172 Italian national seismic hazard model and locally refined by more detailed studies
173 (Boncio et al., 2011; Peruzza et al., 2011; Ferranti et al., 2014).

174 Based on the compiled database, we explored three main aspects associated with
175 defining a fault source input: the slip rate evaluation, the segmentation model and
176 the expected seismicity rate calculation.

177 *2.1.1 Slip rates*

178 Slip rates control fault-based seismic hazards (Main, 1996, Roberts et al., 2004; Bull
179 et al., 2006; Visini and Pace, 2014) and reflect the velocities of the mechanisms that
180 operate during continental deformation (e.g., Cowie et al., 2005). Moreover, long-
181 term observations of faults in various tectonic contexts have shown that slip rates
182 vary in space and time (e.g., Bull et al., 2006; Nicol et al., 2006, 2010, McClymont et
183 al., 2009a-b; Gunderson et al., 2013; Benedetti et al., 2013, D'Amato et al., 2016),
184 and numerical simulations (e.g., Robinson et al., 2009; Cowie et al., 2012; Visini and
185 Pace, 2014) suggest that variability mainly occurs in response to interactions
186 between adjacent faults. Therefore, understanding the temporal variability in fault slip
187 rates is a key point in understanding the earthquake recurrence rates and their
188 variability.

189 To evaluate the minimum and maximum slip rates, that we assumed representatives
190 of the long-term slip rate variability over time, we used slip rates determined in
191 different ways and at different time scales (e.g., at the decadal scale based on
192 geodetic data or at longer scales based on the displacement of Holocene or Plio-
193 Pleistocene horizons). These values were derived from approximately 65 available

194 neotectonics, palaeoseismology and seismotectonics papers (see the supplemental
195 files). In this work, we used the mean of the minimum and maximum slip rate values
196 listed in Table 1 and assumed that they are representative of the long-term
197 behaviour (over the past 15 ky in the Apennines). Because a direct comparison of
198 slip rates over different time intervals obtained by different methods may be
199 misleading (Nicol et al., 2009), we cannot exclude the possibility that uncertainties
200 and errors compilation could affect the original data in some cases. The discussion
201 of these possible biases and their evaluation via statistically derived approaches
202 (e.g., Gardner et al., 1987; Finnegan et al., 2014; Gallen et al., 2015) is beyond the
203 scope of this paper and will be explored in future work. Moreover, we are assuming
204 that slip rate values used are representative of seismic movements, and aseismic
205 factors are not taken into account. Therefore, we believe that investigating the effect
206 of this assumption could be another issue explored in future work; for example, by
207 differentiating between aseismic slip factors in different tectonic contexts.

208 Because 28 faults had no measured slip (or throw) rate (Fig. 1a), we proposed a
209 statistically derived approach to assign a slip rate to these faults. Based on the slip
210 rate spatial distribution shown in Figure 1b, we subdivided the fault database into
211 three large regions—the Northern Apennines, Central-Southern Apennines and
212 Calabria-Sicilian coast—and analysed the slip rate distribution in these three areas.
213 Figure 1b indicates that the slip rates tend to increase from north to south. The fault
214 slip rates in the Northern Apennines range from 0.3 to 0.8 mm/yr, with the most
215 common values ranging from approximately 0.5-0.6 mm/yr; the slip rates in the
216 Central-Southern Apennines range from 0.3 to 1.0, and the most common rate is
217 approximately 0.3 mm/yr; and the slip rates in the southern area (Calabria and Sicily)
218 range from 0.9 to 1.8, with the most common being approximately 0.9 mm/yr.

219 Keeping in mind that average and minimum-maximum range of slip rate represents
220 two different aspects of the slip rate behaviour of a fault (average long-term and its
221 variability), we analysed them independently to assign values to active faults without
222 measures.

223 The first step in assigning an average slip rate and a range of variability to the faults
224 with unknown values is to identify the most representative distribution among known
225 probability density functions using the slip rate data from each of the three areas. We
226 test five well-known probability density functions (*Weibull*, *normal*, *exponential*,

227 *Inverse Gaussian* and *gamma*) against mean slip rate observations. The resulting
228 function with the highest log-likelihood is the *normal* function in all three areas. Thus,
229 the mean value of the *normal* distribution is assigned to the faults with unknown
230 values. We assign a value of 0.58 mm/yr to faults in the northern area, 0.64 mm/yr to
231 faults in the Central-Southern area, and 1.10 mm/yr to faults in the Calabria-Sicilian
232 area. To assign a range of slip rate variability to each of the three areas, we test the
233 same probability density functions against slip rate variability observations. Similar to
234 the mean slip rate, the probability density function with the highest log-likelihood is
235 the *normal* function in all three areas. We assign a variability of 0.25 mm/yr to the
236 faults in the northern area, 0.29 mm/yr to the faults in the Central-Southern area, and
237 0.35 mm/yr to the faults in the Calabria-Sicilian area.

238

239 2.1.2 Segmentation rules for delineating fault sources

240 An important issue in the definition of a fault source input is the formulation of
241 segmentation rules. In fact, the question of whether structural segment boundaries
242 along multisegment active faults act as persistent barriers to a single rupture is
243 critical to defining the maximum seismogenic potential of fault sources. In our case,
244 the rationale behind the definition of a fault source is based on the assumption that
245 the geometric and kinematic features of a fault source are expressions of its
246 seismogenic potential and that its dimensions are compatible for hosting major (M_w
247 ≥ 5.5) earthquakes. Therefore, a fault source may consist of a fault or an ensemble
248 of faults that slip together during an individual major earthquake. A fault source is
249 defined by a *seismogenic master fault* and its surface projection (Fig. 2a).
250 *Seismogenic master faults* are separated from each other by first-order structural or
251 geometrical complexities. Following the suggestions by Boncio et al. (2004) and
252 Field et al. (2015), we imposed the following segmentation rules in our case study: (i)
253 4-km fault gaps among aligned structures; (ii) intersections with cross structures
254 (often transfer faults) extending 4 km along strike and oriented at nearly right angles
255 to the intersecting faults; (iii) overlapping or underlapping en echelon arrangements
256 with separations between faults of 4 km; (iv) bending $\geq 60^\circ$ for more than 4 km; (v)
257 average slip rate variability along a strike greater than or equal to 50%; and (vi)

258 changes in seismogenic thickness greater than 5 km among aligned structures.
259 Example applications of the above rules are illustrated in Figure 2a.

260 By applying the above rules to our fault database, the 110 faults yielded 86 fault
261 sources: 9 strike-slip sources and 77 normal-slip sources. The longest fault source is
262 *Castelluccio dei Sauri* (fault number (*id in Table 1*) 42, L = 93.2 km), and the shortest
263 is *Castrovillari* (*id* 63, L = 10.3 km). The mean length is 30 km. The dip angle varies
264 from 30° to 90°, and 70% of the fault sources have dip angles between 50° and 60°.
265 The mean value of seismogenic thickness (ST) is approximately 12 km. The source
266 with the largest ST is *Mattinata* (*id* 41, ST = 25 km), and the source with the thinnest
267 ST is *Monte Santa Maria Tiberina* (*id* 9, ST = 2.5 km). This low value is due to the
268 presence of an east-dipping low angle normal fault, the Alto-Tiberina Fault (Boncio et
269 al., 2000), located a few kilometres west of the Monte Santa Maria Tiberina fault.
270 Maximum observed moment magnitude values (MObs) have been assigned to 35
271 fault sources (based on Table 2), and the values vary from 5.90 to 7.32. The fault
272 source inputs are shown in Figure 3.

273

274 *2.1.3 Expected seismicity rates*

275 Each fault source is characterized by data, such as kinematic, geometry and slip rate
276 information, that we use as inputs for the FiSH code (Pace et al., 2016) to calculate
277 the global budget of the seismic moment rate allowed by the structure. This
278 calculation is based on predefined size-magnitude relationships in terms of the
279 maximum magnitude (Mmax) and the associated mean recurrence time (Tmean).
280 Table 1 summarizes the geometric parameters used as FiSH input parameters for
281 each fault source (seismogenic box) shown in Figure 3. To evaluate Mmax of each
282 source, according to Pace et al., (2016) we first computed and then combined up to
283 five Mmax estimates (see the example of the Paganica fault source in Fig. 2b, details
284 in Pace et al., 2016). Specifically, these five Mmax estimates are as follows: MM0
285 based on the calculated scalar seismic moment (M0) and the application of the
286 standard formula $M_w = 2/3 (\log M_0 - 9.1)$ (Hanks and Kanamori, 1979; IASPEI,
287 2005); two magnitude estimates using the Wells and Coppersmith (1994) empirical
288 relationships for the maximum subsurface rupture length (MRLD) and maximum
289 rupture area (MRA); a estimate that corresponds to the MObs, if available; and a

290 estimate (MASP, ASP for aspect ratio) computed by reducing the fault length input if
291 the aspect ratio (W/L) is smaller than the value evaluated by the relation between the
292 aspect ratio and rupture length of observed earthquake ruptures, as derived by
293 Peruzza and Pace (2002) (not in the case of Paganica in Fig. 2b). In some cases,
294 the use of MObs it was useful to better constrain the seismogenic potential of
295 individual seismogenic sources. For this reason and to take into account Mobs in the
296 estimation of Mmax, for each source we (i) calculated the maximum expected
297 magnitude (Mmax1) and the relative uncertainties using only the scaling
298 relationships and (ii) compared the maximum of observed magnitudes of the
299 earthquakes potentially associated with the fault. If MObs was within the range of
300 $M_{max} \pm 1$ standard deviation, we considered the value and recalculated a new
301 Mmax (Mmax2) with a new uncertainty. If MObs was larger than $M_{max1} + 1$
302 standard deviation, we reviewed the fault geometry and/or the earthquake-source
303 association. Conversely, if Mobs was lower than $M_{max1} - 1$ standard deviation we
304 considered a GR behaviour for that source, without using the Mobs in the Mmax2
305 calculation. As an example, for the Irpinia Fault (id 51 in Tables 1 and 2), the
306 characteristics of the 1980 earthquake ($M_w \sim 6.9$) can be used to evaluate Mmax via
307 comparison with the Mmax derived from scaling relationships.

308 Because all the empirical relationships, as well as observed historical and recent
309 magnitudes of earthquakes, are affected by uncertainties, the *MomentBalance* (MB)
310 function of the FiSH code (Pace et al., 2016) was used to account for these
311 uncertainties. MB computes a probability density function (PDF) for each magnitude
312 derived from empirical relationships or observations and summarizes the results as a
313 maximum magnitude value with a standard deviation. The uncertainties in the
314 empirical scaling relationship, in FiSH, are taken from the studies of Wells and
315 Coppersmith (1994), Peruzza and Pace (2002) and Leonard (2010). Currently, the
316 uncertainty in magnitude associated with the seismic moment is fixed and set to 0.3,
317 whereas the catalogue defines the uncertainty in MObs. Moreover, to combine the
318 evaluated maximum magnitudes, MB creates a probability curve for each magnitude
319 by assuming a normal distribution (Fig. 2). We assumed a two-sides untruncated
320 normal distribution of magnitudes. MB subsequently sums the probability density
321 curves and fits the summed curve to a normal distribution to obtain the mean of the
322 maximum magnitude M_{max} and its standard deviation.

323 Thus, a unique M_{max} with a standard deviation is computed for each source, and this
324 value represents the maximum rupture that is allowed by the fault geometry and the
325 rheological properties.

326 Finally, to obtain the mean recurrence time of M_{max} (i.e., T_{mean}), we use the criterion
327 of “segment seismic moment conservation” proposed by Field et al. (1999). This
328 criterion divides the seismic moment that corresponds to M_{max} by the moment rate
329 for given a slip rate:

$$330 \quad T_{mean} = \frac{1}{Char_Rate} = \frac{10^{(1.5 M_{max} + 9.1)}}{\mu VLW} \quad (1)$$

331 where T_{mean} is the mean recurrence time in years, $Char_Rate$ is the annual mean
332 rate of occurrence, M_{max} is the computed mean maximum magnitude, μ is the shear
333 modulus, V is the average long-term slip rate, and L and W are along-strike rupture
334 length and downdip width, respectively. Finally, we calculated the seismic moment
335 rate corresponding to M_{max} and the MFDs of expected seismicity. For each fault
336 source, we use two “end-member” MFD models: (i) a *Characteristic Gaussian (CHG)*
337 model, a symmetric Gaussian curve (applied to the incremental MFD values) centred
338 on the M_{max} value of each fault with a range of magnitudes equal to 1-sigma, and (ii)
339 a *Truncated Gutenberg-Richter (TGR, Ordaz, 1999; Kagan, 2002)* model, with M_{max}
340 as the upper threshold and $M_w = 5.5$ as the minimum threshold for all sources. We
341 consider a constant b-value equal to 1.0 for all faults, as single-source events are
342 insufficient for calculating the required statistics; this value corresponds to the mean
343 b-value determined from the CPT15 catalogue. The a-values were computed with
344 the ActivityRate tool of the FiSH code. ActivityRate calculated activity rates at
345 magnitudes given by each MFD, balancing the total MFD expected seismic moment
346 rate with the seismic moment rate that was obtained based on M_{max} and T_{mean}
347 (details in Field et al., 1999; Field et al., 2015; Pace et al., 2016; Woessner et al.,
348 2015). In Figure 2c, we show an example of the expected seismicity rates in terms of
349 the annual cumulative rates for the Paganica source using the two above-described
350 MFD models.

351 Finally, we create a so-called “expert judgement” model, called the *Mixed* model, to
352 determine the MFD for each fault source based on the earthquake-source
353 associations. In this case, we decided that if an earthquake assigned to a fault

354 source (see Table 2 for earthquake-source associations) has a magnitude lower than
355 the magnitude range in the curve of the *CHG* model distribution, the *TGR* model is
356 applied to that fault source. Otherwise, the *CHG* model, which peaks at the
357 calculated M_{max} , is applied. We decided to not use a logic tree for every fault to
358 capture the model options because one of the aims of this work is to compare the
359 different MFD choices in terms of results and impact in the hazard curves. Of course,
360 errors in this approach can originate from the misallocation of historical earthquakes,
361 and we cannot exclude the possibility that potentially active faults responsible for
362 historical earthquakes have not yet been mapped. The MFD model assigned to each
363 fault source in our *Mixed* model is shown in Figure 3.

364

365 **2.2 Distributed Source Inputs**

366 Introducing distributed earthquakes into the seismogenic source model is necessary
367 because researchers have not been able to identify a causative source (i.e., a
368 mapped fault) for important earthquakes in the historical catalogue. This lack of
369 correlation between earthquakes and faults may be related to (i) interseismic strain
370 accumulation in areas between major faults, (ii) earthquakes occurring on unknown
371 or blind faults, (iii) earthquakes occurring on unmapped faults characterized by slip
372 rates lower than the rates of erosional processes, and/or (iv) the general lack of
373 surface ruptures associated with faults generating $M_w < 5.5$ earthquakes.

374 We used the historical catalogue of earthquakes (CPTI15; Rovida et al., 2016; Fig.
375 4) to model the occurrence of moderate-to-large ($M_w \geq 4.5$) earthquakes. The
376 catalogue consists of 4,427 events and covers approximately the last one thousand
377 years from 01/01/1005 to 28/12/2014. Before using the catalogue, we removed all
378 events not considered mainshocks via a declustering filter (Gardner and Knopoff,
379 1974). This process resulted in a catalogue composed of 1,839 independent events,
380 which we denote as the “complete” catalogue. Moreover, to avoid double counting
381 due to the use of two seismicity sources, i.e., the fault sources and the distributed
382 seismicity sources, we removed events associated with known active faults from the
383 CPTI15 earthquake catalogue. If the causative fault of an earthquake is known, that
384 earthquake does not need to be included in the seismicity smoothing procedure. The
385 earthquake-source association is based on neotectonics, palaeoseismology and

386 seismotectonics papers (see the supplemental files) and, in a few cases,
 387 macroseismic intensity maps. In Table 2, we listed the earthquakes with known
 388 causative fault sources. The differences in the smoothed rates given by eq. (2) using
 389 the complete and modified catalogues are shown in Figure 5.

390 We applied the standard methodology developed by Frankel (1995) to estimate the
 391 density of seismicity in a grid with latitudinal and longitudinal spacing of 0.05° . The
 392 smoothed rate of events in each cell i is determined as follows:

$$393 \quad n_i = \frac{\sum_j n_j e^{-\frac{\Delta_{ij}^2}{c^2}}}{\sum_j e^{-\frac{\Delta_{ij}^2}{c^2}}} \quad (2)$$

394 where n_i is the cumulative rate of earthquakes with magnitudes greater than the
 395 completeness magnitude M_c in each cell i of the grid and Δ_{ij} is the distance between
 396 the centres of grid cells i and j . The parameter c is the correlation distance. The sum
 397 is calculated in cells j within a distance of $3c$ of cell i .

398 To compute earthquake rates, we adopted the completeness magnitude thresholds
 399 over different periods given by Stucchi et al. (2011) for five large zones (Fig. 4).

400 To optimize the smoothing distance Δ in eq. (2), we divided the earthquake
 401 catalogue into four 10-yr disjoint learning and target periods from the 1960s to the
 402 1990s. For each pair of learning and target catalogues, we used the probability gain
 403 per earthquake to find the optimal smoothing distance (Kagan and Knopoff, 1977;
 404 Helmstetter et al., 2007). After assuming a spatially uniform earthquake density
 405 model as a reference model, the probability gain per earthquake G of a candidate
 406 model relative to a reference model is given by the following equation:

$$407 \quad G = \exp\left(\frac{L-L_0}{N}\right) \quad (3)$$

408 where N is the number of events in the target catalogue and L and L_0 are the joint
 409 log-likelihoods of the candidate model and reference model, respectively. Under the
 410 assumption of a Poisson earthquake distribution, the joint log-likelihood of a model is
 411 given as follows:

412
$$L = \sum_{i_x=1}^{N_x} \sum_{j_y=1}^{N_y} \log p [\lambda(i_x, i_y), \omega] \quad (4)$$

413 where p is the Poisson probability, λ is the spatial density, ω is the number of
 414 observed events during the target period, and the parameters i_x and i_y denote each
 415 corresponding longitude-latitude cell.

416 Figure 6 shows that for the four different pairs of learning-target catalogues, the
 417 optimal smoothing distance c (the mean curve) ranges from 25-40 km. Finally, the
 418 mean of all the probability gains per earthquake yields a maximum smoothing
 419 distance of 30 km (Fig. 6), which is then used in eq. (2).

420 The b-value of the GR distribution is calculated on a regional basis using the
 421 maximum-likelihood method of Weichert (1980), which allows multiple periods with
 422 varying completeness levels to be combined. Following the approach recently
 423 proposed by Kamer and Hiemer (2015), we used a penalized likelihood-based
 424 method for the spatial estimation of the GR b-values based on the Voronoi
 425 tessellation of space without tectonic dependency. The whole Italian territory has
 426 been divided into a grid with a longitude/latitude spacing of 0.05° , and the centres of
 427 the grid cells represent the possible centres of Voronoi polygons. We vary the
 428 number of Voronoi polygons, N_v , from 3 to 50, generating 1000 tessellations for
 429 each N_v . The summed log-likelihood of each obtained tessellation is compared with
 430 the log-likelihood given by the simplest model (prior model) obtained using the entire
 431 earthquake dataset. We find that 673 random realizations led to better performance
 432 than the prior model. Thus, we calculate an ensemble model using these 673
 433 solutions, and the mean b-value of each grid node is shown in Figure 4.

434 The maximum magnitude M_{max} assigned to each node of the grid, the nodal planes
 435 and the depths have been taken from ESHM13 (Woessner et al., 2015). The
 436 ESHM13 project evaluated the maximum magnitudes of large areas of Europe
 437 based on a joint procedure involving historical observations and tectonic
 438 regionalization. We adopted the lowest value of the maximum magnitude
 439 distributions proposed by ESHM13, but evaluating the impact of different maximum
 440 magnitudes is beyond the scope of this work.

441 Finally, the rates of expected seismicity for each node of the grid are assumed to
442 follow the TGR model (Kagan 2002):

$$443 \quad \lambda(M) = \lambda_0 \frac{\exp(-\beta M) - \exp(-\beta M_u)}{\exp(-\beta M_0) - \exp(-\beta M_u)} \quad (5)$$

444 where the magnitude (M) is in the range of M_0 (minimum magnitude) to M_u (upper or
445 maximum magnitude); otherwise $\lambda(M)$ is 0. Additionally, λ_0 is the smoothed rate of
446 earthquakes at $M_w = 4.5$ and $\beta = b \ln(10)$.

447 **2.3 Combining Fault and Distributed Sources**

448 To combine the two source inputs, we introduced a distance-dependent linear
449 weighting function, such that the contribution from the distributed sources linearly
450 decreases from 1 to 0 with decreasing distance from the fault. The expected
451 seismicity rates of the distributed sources start at $M_w = 4.5$, which is lower than the
452 minimum magnitude of the fault sources, and the weighting function is only
453 applicable in the magnitude range overlapping the MFD of each fault. This weighting
454 function is based on the assumption that faults tend to modify the surrounding
455 deformation field (Fig. 7), and this assumption is explained in detail later in this
456 paper.

457 During fault system evolution, the increase in the size of a fault through linking with
458 other faults results in an increase in displacement that is proportional to the quantity
459 of strain accommodated by the fault (Kostrov, 1974). Under a constant regional
460 strain rate, the activity of fault sections arranged across strike must eventually
461 decrease (Nicol et al., 1997; Cowie, 1998; Roberts et al., 2004). Using an analogue
462 modelling, Mansfield and Cartwright (2001) showed that faults grow via cycles of
463 overlap, relay formation, breaching and linkage between neighbouring segments
464 across a wide range of scales. During the evolution of a system, the merging of
465 neighbour faults, mostly along strike, results in the formation of major faults, which
466 accommodate the majority of displacement. These major faults are surrounded by
467 minor faults, which accommodate lower amounts of displacement. To highlight the
468 spatial patterns of major and minor faults, Figures 7a and 7b present diagrams from
469 the Mansfield and Cartwright (2001) experiment in two different stages: the
470 approximate midpoint of the sequence and the end of the sequence. Numerical
471 modelling performed by Cowie et al. (1993) yielded similar evolutionary features for

472 major and minor faults. The numerical fault simulation of Cowie et al. (1993) was
473 able to reproduce the development of a normal fault system from the early nucleation
474 stage, including interactions with adjacent faults, to full linkage and the formation of a
475 large thoroughgoing fault. The model also captures the increase in the displacement
476 rate of a large linked fault. In Figures 7c and 7d, we focus on two stages of the
477 simulation (from Cowie et al., 1993): the stage in which the fault segments have
478 formed and some have become linked and the final stage of the simulation.

479 Notably, the spatial distributions of major and minor faults are very similar in the
480 experiments of both Mansfield and Cartwright (2001) and Cowie et al. (1993), as
481 shown in Figures 7a-d. Developments during the early stage of major fault formation
482 appear to control the location and evolution of future faults, with some areas where
483 no major faults develop. The long-term evolution of a fault system is the
484 consequence of the progressive cumulative effects of the slip history, i.e.,
485 earthquake occurrence, of each fault. Large earthquakes are generally thought to
486 produce static and dynamic stress changes in the surrounding areas (King et al.,
487 1994; Stein, 1999; Pace et al., 2014; Verdecchia and Carena, 2016). Static stress
488 changes produce areas of negative stress, also known as shadow zones, and
489 positive stress zones. The spatial distributions of decreases (unloading) and
490 increases (loading) in stress during the long-term slip history of faults likely influence
491 the distance across strike between major faults. Thus, given a known major active
492 fault geometrically capable of hosting a $M_w \geq 5.5$ earthquake, the possibility that a
493 future $M_w \geq 5.5$ earthquake will occur in the vicinity of the fault, but is not caused by
494 that fault, should decrease as the distance from the fault decreases. Conversely,
495 earthquakes with magnitudes lower than 5.5 and those due to slip along minor faults
496 are likely to occur everywhere within a fault system, including in proximity to a major
497 fault.

498 In Figure 7e, we illustrate the results of the analogue and numerical modelling of
499 fault system evolution and indicate the areas around major faults where it is unlikely
500 that other major faults develop. In Figure 7f, we show the next step in moving from
501 geologic and structural considerations. In this step, we combine fault sources and
502 distributed seismicity source inputs, which serve as inputs of the seismogenic model.
503 Fault sources are used to model major faults and are represented by a master fault
504 (i.e., one or more major faults) and its projection at the surface. Distributed seismicity
505 is used to model seismicity associated with minor, unknown or unmapped faults.

506 Depending on the positions of distributed seismicity points with respect to the buffer
 507 zones around major faults, the rates of expected distributed seismicity remain
 508 unmodified or decrease and can even reach zero.

509 Specifically, we introduced a slip rate and a distance-weighted linear function based
 510 on the above reasoning. The probability of the occurrence of an earthquake (Pe) with
 511 a M_w greater than or equal to the minimum magnitude of the fault is as follows:

$$512 \quad Pe = \begin{cases} 0, & d \leq 1 \text{ km} \\ d/d_{max}, & 1 \text{ km} < d \leq d_{max} \\ 1, & d > d_{max} \end{cases} \quad (6)$$

513 where d is the Joyner-Boore distance from a fault source. The maximum value of d
 514 (d_{max}) is assumed to be controlled by the slip rate of the fault. For faults with slip
 515 rates ≥ 1 mm/yr, we assume $d_{max} = L/2$ (L is the length along the strike, Fig. 2a); for
 516 faults with slip rates of 0.3 - 1 mm/yr, $d_{max} = L/3$; and for faults with slip rates of ≤ 0.3
 517 mm/yr, $d_{max} = L/4$. The rationale for varying d_{max} is given by a simple assumption: the
 518 higher the slip rate is, the larger the deformation field and the higher the value of
 519 d_{max} . This linear function has been applied around each fault, without differences
 520 between footwall and hangingwall. We applied eq. (6) to the smoothed occurrence
 521 rates of the distributed seismogenic sources. In Figure 8 we show the annual
 522 cumulative MFD (Fig. 8a) and incremental annual MFD (Fig. 8c) computed for the
 523 red bounded area in Figure 8b. Because we consider three fault source inputs (red
 524 lines in Fig.8): one using only TGR MFD; one using only CHG MFD; and one using
 525 *Mixed model* MFD and because the MFDs of distributed seismicity grid points in the
 526 vicinity of faults are modified with respect to the MFDs of these faults, we obtain
 527 three different inputs of distributed seismicity (blue lines in Fig. 8). These three
 528 distributed seismogenic source inputs differ because the minimum magnitude of the
 529 faults is M_w 5.5 in the TGR model, but this value depends on each fault source
 530 dimension in the CHG and Mixed model. From $M_w = 4.5$ to $M_w = 5.5$ the complete
 531 CPT15 is fully described by the MFD of the distributed source input. From $M_w = 5.5$
 532 to $M_w = 6.3$ the total MFD (black lines in Fig. 8) computed using only TGR MFD is
 533 higher than the MFD computed using only CHG and Mixed MFD, this because the
 534 annual rates of occurrences of intermediate-magnitude events obtained with TGR
 535 model are higher than the ones obtained with CHG and Mixed model, as shown in
 536 the incremental annual MFD in Figure 8c. From $M_w = 6.4$ to $M_w = 7.3$ the total MFDs

537 computed using only CHG and Mixed MFD are higher the total MFD obtained with
538 TGR model.

539 Our approach allows incompleteness in the fault database to be bypassed, which is
540 advantageous because all fault databases should be considered incomplete. In our
541 approach, the seismicity is modified only in the vicinity of mapped faults. The
542 remaining areas are fully described by the *distributed* input. With this approach, we
543 do not define regions with reliable fault information, and the locations of currently
544 unknown faults can be easily included when they are discovered in the future.

545 **3. Results and Discussion**

546 To probabilistically obtain ground shaking, we assign the calculated seismicity rates,
547 based on the Poisson hypothesis, to their pertinent geometries, i.e., individual 3D
548 seismogenic sources for the *fault input* and point sources for the *distributed input*
549 (Fig. 8). All the computations are performed using the OpenQuake Engine, an open
550 source software developed recently with the purpose of providing seismic hazard
551 and risk assessments (Pagani et al., 2014). Moreover, it is widely recognized within
552 the scientific community for its potential. The ground motion prediction equations
553 (GMPE) of Akkar et al. (2013), Chiou et al., (2008), Faccioli et al., (2010) and Zhao
554 et al., (2006) are used, because these GMPEs were selected in the ESHM13
555 (Woessner et al., 2015) for active shallow crust. In addition, we used the GMPE
556 proposed by Bindi et al. (2014) and calibrated using Italian data. We combined all
557 GMPEs into a logic tree with the same weight of 0.2 for each branch. Note that these
558 GMPEs use different distance metrics: the Joyner and Boore distance for Akkar et al.
559 (2013), Bindi et al. (2014) and Chiou et al. (2008) and the closest rupture distance
560 for Faccioli et al. (2010) and Zhao et al. (2006).

561 The results of the fault source inputs, distributed source inputs, and aggregated
562 model are expressed in terms of peak ground acceleration (PGA) for exceedance
563 probabilities of 10% and 2% over 50 years, corresponding to return periods of 475
564 and 2,475 years, respectively (Fig. 9).

565 To explore the epistemic uncertainty associated with the MFDs of fault source inputs,
566 we compared the seismic hazard levels obtained based on the TGR and CHG fault
567 source inputs (left column in Fig. 9) using the TGR and CHG MFDs for all the fault

568 sources (details in section 2.1.3). Although both models have the same seismic
569 moment release, the different MFDs generate clear differences. In fact, for 10%
570 exceedance probability in 50 yr, in the *TGR* model all faults contribute significantly to
571 the seismic hazard level, whereas in the *CHG* model, only a few faults located in the
572 central Apennines and Calabria contribute to the seismic hazard level. This
573 difference is due to the different shapes of the MFDs in the two models (Fig. 2c). As
574 shown in Figure 8, the amount of earthquakes with magnitudes between 5.5 and
575 approximately 6, which are likely the main contributors to these levels of seismic
576 hazard, is generally higher in the *TGR* model than in the *CHG* model. At a 2%
577 probability of exceedance in 50 years, all fault sources in the *CHG* contribute to the
578 seismic hazard level, but the absolute values are still generally higher in the *TGR*
579 model.

580 The *distributed input* (middle column in Fig. 9) depicts a more uniform shape of the
581 seismic hazard level than that of fault source inputs. A PGA value lower than 0.125 g
582 at a 10% probability of exceedance over 50 years and lower than 0.225 g at a 2%
583 probability of exceedance over 50 years encompass a large part of peninsular Italy
584 and Sicily. Two areas with high levels of ground shaking are located in the central
585 Apennines and northeastern Sicily.

586 The overall model, which was obtained by combining the fault and distributed source
587 inputs, is shown in the right column of Figure 9. Areas with comparatively high
588 seismic hazard levels, i.e., hazard levels greater than 0.225 g and greater than 0.45
589 g at 50-yr exceedance probabilities of 10% and 2%, respectively, are located
590 throughout the Apennines, in Calabria and in Sicily. The fault source inputs
591 contribute most to the total seismic hazard levels in the Apennines, Calabria and
592 eastern Sicily, where the highest PGA values are observed.

593 Figure 10 shows the ratios to the total seismic hazard level by the *fault* and
594 *distributed* source inputs at a specific site (L'Aquila, 42.400-13.400). Notably, in
595 Figure 10, *distributed* sources dominate the seismic hazard contribution at
596 exceedance probabilities greater than ~81% over 50 years, but the contribution of
597 *fault* sources cannot be neglected. Conversely, at exceedance probabilities of less
598 than ~10% in 50 years, the total hazard level is mainly associated with *fault* source
599 inputs. Moreover, note that the contributions are not based on deaggregation but are

600 computed according to the percentage of each source input in the AFOE value of the
601 combined model.

602 Figure 11 presents seismic hazard maps for PGA at 10% and 2% exceedance
603 probabilities in 50 years for *fault* sources, *distributed* sources and a combination of
604 the two. These data were obtained using the above-described *Mixed* model, in which
605 we selected the most “appropriate” MFD model (TGR or CHG) for each fault (as
606 shown in Figure 3). The results of this model therefore have values between those of
607 the two end-members shown in Figure 9.

608 Figure 12 shows the *CHG*, *TGR* and *Mixed* model hazard curves of three sites
609 (Cesena, L’Aquila and Crotone, Fig. 13c). As previously noted, the results of the
610 *Mixed* model, due to the structure of the model, are between those of the *CHG* and
611 *TGR* models. The relative positions of the hazard curves derived from the two end-
612 member models and the *Mixed* model depend on the number of nearby fault sources
613 that have been modelled using one of the MFD models and on the distance of the
614 site from the faults. For example, in the case of the Crotone site, the majority of the
615 fault sources in the *Mixed* model are modelled using the CHG MFD. Thus, the
616 resulting hazard curve is similar to that of the *CHG* model. For the Cesena site, the
617 three hazard curves overlap. Because the distance between Cesena and the closest
618 fault sources is approximately 60 km, the impact of the fault input is less than the
619 impact of the *distributed* source input. In this case, the choice of a particular MFD
620 model has a limited impact on the modelling of *distributed* sources. Notably, for an
621 annual frequency of exceedance (*AFOE*) higher than 10^{-4} , the *TGR fault* source
622 input values are generally higher than those of the *CHG* source input, and the three
623 models converge at *AFOE* lower than 10^{-4} , as shown for L’Aquila site. The resulting
624 seismic hazard estimates depend on the assumed MFD model (*TGR* vs. *CHG*), and
625 for the investigated range of *AFOE*, especially on the annual rates of occurrences of
626 intermediate-magnitude events (5.5 to ~6.5, see Fig. 8). Therefore, the *TGR* model
627 leads to the highest hazard values because this range of magnitude (5.5 to ~ 6.5)
628 contributes the most to the hazard level.

629 In Figure 13, we investigated the influences of the *Mixed fault* source inputs and the
630 *Mixed distributed* source inputs on the total hazard level of the entire study area, as
631 well as the spatial variability. The maps in Figure 13a show that the contribution of

632 *fault* inputs to the total hazard level generally decreases as the exceedance
633 probability increases from 2% to 81% in 50 years. At a 2% probability of exceedance
634 in 50 years, the total hazard levels in the Apennines and eastern Sicily are mainly
635 related to faults, whereas at an 81% probability of exceedance in 50 years, the
636 contributions of *fault* inputs are high in local areas of central Italy and southern
637 Calabria.

638 Moreover, we examined the contributions of *fault* and *distributed* sources along three
639 E-W-oriented profiles in northern, central and southern Italy (Fig. 13b). In areas with
640 faults, the hazard level estimated by *fault* inputs is generally higher than that
641 estimated by the corresponding *distributed* source inputs. Notable exceptions are
642 present in areas proximal to slow-slipping active faults at an 81% probability of
643 exceedance in 50 years (profile A), such as those at the eastern and western
644 boundaries of the fault area in central Italy (profile B), and in areas where the
645 contribution of the *distributed* source input is equal to that of the *fault* input at a 10%
646 probability of exceedance in 50 years (eastern part of profile C).

647 The features depicted by the three profiles result from a combination of the slip rates
648 and spatial distributions of faults for *fault* source inputs. The proposed approach
649 requires a high level of expertise in active tectonics and cautious expert judgement
650 at many levels in the procedure. First, the seismic hazard estimate is based on the
651 definition of a segmentation model, which requires a series of rules based on
652 observations and empirical regression between earthquakes and the size of the
653 causative fault. New data might make it necessary to revise the rules or reconsider
654 the role of the segmentation. In some cases, expert judgement could permit
655 discrimination among different fault source models. Alternatively, all models should
656 be considered branches in a logic tree approach.

657 Moreover, we propose a fault seismicity input in which the MFD of each fault source
658 has been chosen based on an analysis of the occurrences of earthquakes that can
659 be tentatively or confidently assigned to a certain fault. To describe the fault activity,
660 we applied a probability density function to the magnitude, as commonly performed
661 in the literature: the TGR model, where the maximum magnitude is the upper
662 threshold and $M_w = 5.5$ is the lower threshold for all faults, and the characteristic
663 maximum magnitude model, which consists of a truncated normal distribution

664 centred on the maximum magnitude. Other MFDs have been proposed to model the
665 earthquake recurrence of a fault. For example, Youngs and Coppersmith (1985)
666 proposed a modification to the truncated exponential model to allow for the
667 increased likelihood of characteristic events. However, we focused only on two
668 models, as we believe that instead of a “blind” or qualitative characterization of the
669 MFD of a fault source, future applications of statistical tests of the compatibility
670 between expected earthquake rates and observed historical seismicity could be used
671 as an objective method of identifying the optimal MFD of expected seismicity. As
672 shown in this analyses, fault sources, even if modelled by TGR or CHG MFD, are
673 able to match occurred seismicity for magnitude \sim 5.5 (see for example Fig. 8) and
674 so are complementary to other inputs that model seismicity using area sources or
675 smoothing approaches.

676 To focus on the general procedure for spatially integrating faults with sources
677 representing distributed (or off-fault) seismicity, we did not investigate the impact of
678 other smoothing procedures on the distributed sources, and we used fixed kernels
679 with a constant bandwidth (as in the works of Kagan and Jackson, 1994; Frankel et
680 al. 1997; Zechar and Jordan, 2010). The testing of adaptive bandwidths (e.g., Stock
681 and Smith, 2002; Helmstetter et al., 2006, 2007; Werner et al., 2010; Hiemer et al,
682 2014) or weighted combinations of both models has been reserved for future studies.

683

684 Finally, we compared, as shown in Figure 14, the 2013 European Seismic Hazard
685 Model (ESHM13) developed within the SHARE project, the current Italian national
686 seismic hazard map (MPS04) and the results of our model (Mixed model) using the
687 same GMPEs as used in this study. Specifically, for ESHM13, we compared the
688 results to the fault-based hazard map (FSBG model) that accounts for fault sources
689 and background seismicity. The figure shows how the impact of our fault sources is
690 more evident than in FSBG-ESHM13, and the comparison with MPS04 confirms a
691 similar pattern, but with some significant differences at the regional to local scales.

692

693 The strength of our approach lies in the integration of different levels of information
694 regarding the active faults in Italy, but the final result is unavoidably linked to the
695 quality of the relevant data. Our work focused on presenting and applying a new
696 approach for evaluating seismic hazards based on active faults and intentionally

697 avoided the introduction of uncertainties due to the use of different segmentation
698 rules or other slip rate values of faults. Moreover, the impact of ground motion
699 predictive models is important in seismic hazard assessment but beyond the scope
700 of this work. Future steps will be devoted to analysing these uncertainties and
701 evaluating their impacts on seismic hazard estimates.

702

703 **4. Conclusions**

704 We presented a seismogenic source model for Italy, which summarizes and
705 integrates the fault-based models developed within the last decade (Pace et al.,
706 2006).

707 The model proposed in this study combines fault source inputs based on over 110
708 faults grouped into 86 fault sources and distributed source inputs. For each fault
709 source, the maximum magnitude and its uncertainty were derived by applying
710 scaling relationships, and the rates of seismic activity were derived by applying slip
711 rates to seismic moment evaluations and balancing these seismic moments using
712 two MFD models.

713 To account for unknown faults, a distributed seismicity input was applied following
714 the well-known Frankel (1995) methodology to calculate seismicity parameters.

715 The fault sources and gridded distributed seismicity sources have been integrated
716 via a new approach based on the idea that deformation in the vicinity of an active
717 fault is concentrated along the fault and that the seismic activity in the surrounding
718 region is reduced. In particular, a distance-dependent linear weighting function has
719 been introduced to allow the contribution of distributed sources (in the magnitude
720 range overlapping the MFD of each fault source) to linearly decrease from 1 to 0 with
721 decreasing distance from a fault. The strength of our approach lies in the ability to
722 integrate different levels of available information for active faults that actually exist in
723 Italy (or elsewhere), but the final result is unavoidably linked to the quality of the
724 relevant data. We think that our seismogenic source model includes significant
725 advances in the use of integrated active fault and seismological data.

726 The probabilistically estimated ground shaking maps produced using our model
727 show a hazard pattern similar to that of the current maps at the national scale, but
728 some significant differences in hazard level are present at the regional to local scales

729 (Figure 13).

730 Moreover, the impact of using different MFD models to derive seismic activity rates
731 has on the hazard maps was investigated. The PGA values in the hazard maps
732 obtained with the *TGR* model are higher than those in the hazard maps based on the
733 *CHG* model. This difference is because the rates of earthquakes with magnitudes
734 from 5.5 to approximately 6 are generally higher in the *TGR* model than in the *CHG*
735 model. Moreover, the relative contributions of fault source inputs and distributed
736 source inputs have been identified in maps and profiles in three sectors of the study
737 area. These profiles show that the hazard level is generally higher where fault inputs
738 are used, and for high probabilities of exceedance, the contribution of *distributed*
739 inputs equals that of *fault* inputs.

740 Finally, the *Mixed* model was created by selecting the most appropriate MFD model
741 for each fault. All data, including the locations and parameters of fault sources, are
742 provided in the supplemental files of this paper.

743 It shall be noted that our new seismogenic source model is not intended to replace,
744 integrate or assess the current official national seismic hazard model of Italy. While
745 some aspects remain to be implemented in our approach (e.g., the integration of
746 reverse/thrust faults in the database, sensitivity tests for the distance-dependent
747 linear weighting function parameters, sensitivity tests for potential different
748 segmentation models, and fault source inputs that account for fault interactions), the
749 proposed model represents advancements in terms of input data (quantity and
750 quality) and methodology based on a decade of research in the field of fault-based
751 approaches to regional seismic hazard modelling.

752

753

754

755

756

757

758

759 **References**

760

761

762 Akinci, A., Galadini, F., Pantosti, D., Petersen, M., Malagnini, L., and Perkins, D.:
763 Effect of Time Dependence on Probabilistic Seismic-Hazard Maps and
764 Deaggregation for the Central Apennines, Italy, *B Seismol Soc Am*, 99, 585-
765 610, 2009.

766 Akkar, S., Sandikkaya, M.A. , Bommer, J.J.: Empirical Ground-Motion Models for
767 Point and Extended-Source Crustal Earthquake Scenarios in Europe and the
768 Middle East, *Bulletin of Earthquake Engineering*, ISSN:1570-761X, 2013.

769 Benedetti, L., Manighetti, I., Gaudemer, Y., Finkel, R., Malavieille, J., Pou, K., Arnold,
770 M., Aumaitre, G., Bourles, D., and Keddadouche, K.: Earthquake synchrony
771 and clustering on Fucino faults (Central Italy) as revealed from in situ CI-36
772 exposure dating, *J Geophys Res-Sol Ea*, 118, 4948-4974, 2013.

773 Bindi, D., Massa, M., Luzi, L., Ameri, G., Pacor, F., Puglia, R., and Augliera, P.: Pan-
774 European ground-motion prediction equations for the average horizontal
775 component of PGA, PGV, and 5%-damped PSA at spectral periods up to 3.0
776 s using the RESORCE dataset (vol 12, pg 391, 2014), *B Earthq Eng*, 12, 431-
777 448, 2014.

778 Boncio, P., Brozzetti, F. and Lavecchia G.: Architecture and seismotectonics of a
779 regional Low-Angle Normal Fault zone in Central Italy. *Tectonics*, 19 (6),
780 1038-1055, 2000.

781 Boncio, P., Lavecchia, G., and Pace, B.: Defining a model of 3D seismogenic
782 sources for Seismic Hazard Assessment applications: The case of central
783 Apennines (Italy), *J Seismol*, 8, 407-425, 2004.

784 Boncio, P., Pizzi, A., Cavuoto, G., Mancini, M., Piacentini, T., Miccadei, E., Cavinato,
785 G. P., Piscitelli, S., Giocoli, A., Ferretti, G., De Ferrari, R., Gallipoli, M. R.,
786 Mucciarelli, M., Di Fiore, V., Franceschini, A., Pergalani, F., Naso, G., and
787 Macroarea, W. G.: Geological and geophysical characterisation of the
788 Paganica - San Gregorio area after the April 6, 2009 L'Aquila earthquake (M-
789 w 6.3, central Italy): implications for site response, *B Geofis Teor Appl*, 52,
790 491-512, 2011.

791 Bull, J. M., Barnes, P. M., Lamarche, G., Sanderson, D. J., Cowie, P. A., Taylor, S.
792 K., and Dix, J. K.: High-resolution record of displacement accumulation on an
793 active normal fault: implications for models of slip accumulation during
794 repeated earthquakes, *J Struct Geol*, 28, 1146-1166, 2006.

795 Chiou, B. S. J. and Youngs, R. R.: An NGA model for the average horizontal
796 component of peak ground motion and response spectra, *Earthq Spectra*, 24,
797 173-215, 2008.

798 Cornell, C.A.: Engineering seismic risk analysis, *Bull. Seism. Soc. Am.*, 58,1583-
799 1606, 1968.

800 Cowie, P. A., Vanneste, C., and Sornette, D.: Statistical Physics Model for the
801 Spatiotemporal Evolution of Faults, *J Geophys Res-Sol Ea*, 98, 21809-21821,
802 1993.

803 Cowie, P. A.: A healing-reloading feedback control on the growth rate of seismogenic
804 faults, *J Struct Geol*, 20, 1075-1087, 1998.

805 Cowie, P. A., Underhill, J. R., Behn, M. D., Lin, J., and Gill, C. E.: Spatio-temporal
806 evolution of strain accumulation derived from multi-scale observations of Late
807 Jurassic rifting in the northern North Sea: A critical test of models for
808 lithospheric extension, *Earth Planet Sc Lett*, 234, 401-419, 2005.

809 Cowie, P. A., Roberts, G. P., Bull, J. M., and Visini, F.: Relationships between fault
810 geometry, slip rate variability and earthquake recurrence in extensional
811 settings, *Geophys J Int*, 189, 143-160, 2012.

812 D'amato, D., Pace, B., Di Nicola, L., Stuart, F.M., Visini, F., Azzaro, R., Branca, S.,
813 and Barfod, D.N.: Holocene slip rate variability along the Pernicana fault
814 system (Mt. Etna, Italy): Evidence from offset lava flows: *GSA Bulletin*,
815 doi:10.1130/B31510.1, 2016.

816 Danciu, L., Şeşetyan, K., Demircioglu, M. et al.: The 2014 Earthquake Model of the
817 Middle East: seismogenic sources, *Bull Earthquake Eng*,
818 <https://doi.org/10.1007/s10518-017-0096-8>, 2017.

819 Faccioli, E., Bianchini, A., and Villani, M.: New ground motion prediction equations
820 for $t > 1$ s and their influence on seismic hazard assessment, In: *Proceedings*
821 *of the University of Tokyo symposium on long-period ground motion and*
822 *urban disaster mitigation*, 2010.

823 Ferranti, L., Palano, M., Cannavo, F., Mazzella, M. E., Oldow, J. S., Gueguen, E.,
824 Mattia, M., and Monaco, C.: Rates of geodetic deformation across active
825 faults in southern Italy, *Tectonophysics*, 621, 101-122, 2014.

826 Field, E. H., Jackson, D. D., and Dolan, J. F.: A mutually consistent seismic-hazard
827 source model for southern California, *B Seismol Soc Am*, 89, 559-578, 1999.

828 Field, E. H., Jordan, T. H., Page, M. T., Milner, K. R., Shaw, B. E., Dawson, T., Biasi,
829 G. P., Parsons, T., Hardebeck, J. L., Michael, A. J., Weldon, R. J., Powers, P.
830 M., Johnson, K. M., Zeng, Y., Bird, P., Felzer, K. R., van der Elst, N. J.,
831 Madden, C., Arrowsmith, R., Werner, M. J., Thatcher, W. R., & Jackson, D.
832 D.: A Synoptic View of the Third Uniform California Earthquake Rupture
833 Forecast (UCERF3). *Seismological Research Letters*,. doi:
834 [10.1785/0220170045](https://doi.org/10.1785/0220170045), 2017.

835 Field, E. H., Biasi, G. P., Bird, P., Dawson, T. E., Felzer, K. R., Jackson, D. D.,
836 Johnson, K. M., Jordan, T. H., Madden, C., Michael, A. J., Milner, K. R., Page,
837 M. T., Parsons, T., Powers, P. M., Shaw, B. E., Thatcher, W. R., Weldon, R.
838 J., and Zeng, Y. H.: Long-Term Time-Dependent Probabilities for the Third
839 Uniform California Earthquake Rupture Forecast (UCERF3), *B Seismol Soc*
840 *Am*, 105, 511-543, 2015.

841 Finnegan, N. J., Schumer, R., and Finnegan, S.: A signature of transience in bedrock
842 river incision rates over timescales of 10(4)-10(7) years, *Nature*, 505, 391-+,
843 2014.

844 Frankel, A.: Simulating Strong Motions of Large Earthquakes Using Recordings of
845 Small Earthquakes - the Loma-Prieta Mainshock as a Test-Case, *B Seismol*
846 *Soc Am*, 85, 1144-1160, 1995.

847 Frankel, A., Mueller, C., Barnhard, T., Perkins, D., Leyendecker, E. V., Dickman, N.,
848 Hanson, S.. and Hopper, M.: Seismic-hazard maps for California, Nevada,
849 and Western Arizona/Utah', U.S. Geological Survey Open-File Rept. 97-130,
850 1997.

851 Gallen, S. F., Pazzaglia, F. J., Wegmann, K. W., Pederson, J. L., and Gardner, T.
852 W.: The dynamic reference frame of rivers and apparent transience in incision
853 rates, *Geology*, 43, 623-626, 2015.

854 Garcia-Mayordomo, J., Gaspar-Escribano, J. M., and Benito, B.: Seismic hazard
855 assessment of the Province of Murcia (SE Spain): analysis of source
856 contribution to hazard, *J Seismol*, 11, 453-471, 2007.

857 Gardner, J. K., Knopoff, L.: Is the sequence of earthquakes in Southern California,
858 with aftershocks removed, Poissonian?'. *Bulletin of the Seismological Society*
859 *of America*, 64, 1363-1367, 1974.

860 Gardner, T. W., Jorgensen, D. W., Shuman, C., and Lemieux, C. R.: Geomorphic
861 and Tectonic Process Rates - Effects of Measured Time Interval, *Geology*, 15,
862 259-261, 1987.

863 Gasperini P., Bernardini F., Valensise G. and Boschi E.: Defining Seismogenic
864 Sources from Historical Earthquake Felt Reports, *Bull. Seism. Soc. Am.*, 89,
865 94-110, 1999.

866 Gunderson, K. L., Anastasio, D. J., Pazzaglia, F. J., and Picotti, V.: Fault slip rate
867 variability on 10(4)-10(5)yr timescales for the Salsomaggiore blind thrust fault,
868 Northern Apennines, Italy, *Tectonophysics*, 608, 356-365, 2013.

869 Hanks, T. C., and Kanamori, H.: A moment magnitude scale, *Journal of Geophysics*
870 *Research*, 84, 2348–2350, 1979.

871 Helmstetter, A., Kagan, Y. Y., and Jackson, D. D.: Comparison of short-term and
872 time-independent earthquake forecast models for southern California, *B*
873 *Seismol Soc Am*, 96, 90-106, 2006.

874 Helmstetter, A., Kagan, Y. Y., and Jackson, D. D.: High-resolution time-independent
875 grid-based forecast for $M \leq 5$ earthquakes in California, *Seismol Res Lett*,
876 78, 78-86, 2007.

877 Hiemer, S., Woessner, J., Basili, R., Danciu, L., Giardini, D., and Wiemer, S.: A
878 smoothed stochastic earthquake rate model considering seismicity and fault
879 moment release for Europe, *Geophysical Journal International*, Volume 198,
880 Pages 1159–1172, <https://doi.org/10.1093/gji/ggu186>, 2014.

881 International Association of Seismology and Physics of the Earth's Interior (IASPEI):
882 Summary of Magnitude Working Group recommendations on standard
883 procedures for determining earthquake magnitudes from digital data,
884 [http://www.iaspei.org/](http://www.iaspei.org/commissions/CSOI/summary_of_WG_recommendations_2005.pdf)
885 [commissions/CSOI/summary_of_WG_recommendations_2005.pdf](http://www.iaspei.org/commissions/CSOI/summary_of_WG_recommendations_2005.pdf) (last
886 accessed December 2015), 2005.

887 Kagan, Y. Y., Jackson D.D., and Geller, R.J.: Characteristic earthquake model,
888 1884–2011, R.I.P., *Seismol Res Lett*, 83, no. 6, 951– 953, 2012.

889 Kagan, Y., and Knopoff, L.: Earthquake risk prediction as a stochastic process,
890 *Physics of the Earth and Planetary Interiors*, 14, 97–108, 1977.

891 Kagan, Y. Y. and Jackson, D. D.: Long-Term Probabilistic Forecasting of
892 Earthquakes, *J Geophys Res-Sol Ea*, 99, 13685-13700, 1994.

893 Kagan, Y. Y.: Seismic moment distribution revisited: I. Statistical results, *Geophys J*
894 *Int*, 148, 520-541, 2002.

895 Kamer, Y. and Hiemer, S.: Data-driven spatial b value estimation with applications to
896 California seismicity: To b or not to b, *J Geophys Res-Sol Ea*, 120, 5191-
897 5214, 2015.

898 King, G. C. P., Stein, R. S., and Lin, J.: Static Stress Changes and the Triggering of
899 Earthquakes, *B Seismol Soc Am*, 84, 935-953, 1994.

900 Kostrov, V. V.: Seismic moment and energy of earthquakes, and seismic flow of
901 rock, *Physic of the Solid Earth*, 1, 23-44, 1974.

902 Leonard, M.: Earthquake fault scaling: Self-consistent relating of rupture length,
903 width, average displacement, and moment release. *Bulletin of the*
904 *Seismological Society of America*, 100(5A), 1971- 1988, 2010.

905 Machette, M.N.: Active, capable, and potentially active faults; a paleoseismic
906 perspective, *J. Geodyn.*, 29, 387–392, 2000.

907 Main, I.: Statistical physics, seismogenesis, and seismic hazard, *Rev Geophys*, 34,
908 433-462, 1996.

909 Mansfield, C. and Cartwright, J.: Fault growth by linkage: observations and
910 implications from analogue models, *J Struct Geol*, 23, 745-763, 2001.

911 Meletti, C., Visini, F., D'Amico, V., and Rovida A.: Seismic hazard in central Italy and
912 the 2016 Amatrice earthquake, *Annals of Geophysics*, 59, doi:10.4401/ag-
913 7248, 2016.

914 McClymont, A. F., Villamor, P., and Green, A. G.: Assessing the contribution of off-
915 fault deformation to slip-rate estimates within the Taupo Rift, New Zealand,
916 using 3-D ground-penetrating radar surveying and trenching, *Terra Nova*, 21,
917 446-451, 2009a.

918 McClymont, A. F., Villamor, P., and Green, A. G.: Fault displacement accumulation
919 and slip rate variability within the Taupo Rift (New Zealand) based on trench
920 and 3-D ground-penetrating radar data, *Tectonics*, 28, 2009b.

921 Nicol, A., Walsh, J. J., Watterson, J., and Underhill, J. R.: Displacement rates of
922 normal faults, *Nature*, 390, 157-159, 1997.

923 Nicol, A., Walsh, J., Berryman, K., and Villamor, P.: Interdependence of fault
924 displacement rates and paleoearthquakes in an active rift, *Geology*, 34, 865-
925 868, 2006.

926 Nicol, A., Walsh, J., Mouslopoulou, V., and Villamor, P.: Earthquake histories and
927 Holocene acceleration of fault displacement rates, *Geology*, 37, 911-914,
928 2009.

929 Nicol, A., Walsh, J. J., Villamor, P., Seebeck, H., and Berryman, K. R.: Normal fault
930 interactions, paleoearthquakes and growth in an active rift, *J Struct Geol*, 32,
931 1101-1113, 2010.

932 Ordaz, M. and Reyes, C.: Earthquake hazard in Mexico City: Observations versus
933 computations, *B Seismol Soc Am*, 89, 1379-1383, 1999.

934 Pace, B., Peruzza, L., Lavecchia, G., and Boncio, P.: Layered seismogenic source
935 model and probabilistic seismic-hazard analyses in central Italy, *B Seismol*
936 *Soc Am*, 96, 107-132, 2006.

937 Pace, B., Bocchini, G. M., and Boncio, P.: Do static stress changes of a moderate-
938 magnitude earthquake significantly modify the regional seismic hazard? Hints
939 from the L'Aquila 2009 normal-faulting earthquake (Mw 6.3, central Italy),
940 *Terra Nova*, 26, 430-439, 2014.

941 Pace, B., Visini, F., and Peruzza, L.: FiSH: MATLAB Tools to Turn Fault Data into
942 Seismic-Hazard Models, *Seismol Res Lett*, 87, 374-386, 2016.

943 Pagani, M., Monelli, D., Weatherill, G., Danciu, L., Crowley, H., Silva, V., Henshaw,
944 P., Butler, L., Nastasi, M., Panzeri, L., Simionato, M., and Vigano, D.:
945 OpenQuake-engine: an open hazard (and risk) software for the Global
946 Earthquake Model, *Seismol Res Lett* 85:692–702. doi:[10.1785/0220130087](https://doi.org/10.1785/0220130087),
947 2014.

948 Peruzza, L., and Pace B.: Sensitivity analysis for seismic source characteristics to
949 probabilistic seismic hazard assessment in central Apennines (Abruzzo area),
950 *Bollettino di Geofisica Teorica ed Applicata* 43, 79–100, 2002.

951 Peruzza, L., Pace, B., and Visini, F.: Fault-Based Earthquake Rupture Forecast in
952 Central Italy: Remarks after the L'Aquila M-w 6.3 Event, *B Seismol Soc Am*,
953 101, 404-412, 2011.

954 Peruzza, L., Gee, R., Pace, B., Roberts, G., Scotti, O., Visini, F., Benedetti, L., and
955 Pagani, M.: PSHA after a strong earthquake: hints for the recovery, *Annals of*
956 *Geophysics*, 59, doi:10.4401/ag-7257, 2016

957 Roberts, G. P., Cowie, P., Papanikolaou, I., and Michetti, A. M.: Fault scaling
958 relationships, deformation rates and seismic hazards: an example from the
959 Lazio-Abruzzo Apennines, central Italy, *J Struct Geol*, 26, 377-398, 2004.

960 Roberts, G. P. and Michetti, A. M.: Spatial and temporal variations in growth rates
961 along active normal fault systems: an example from The Lazio-Abruzzo
962 Apennines, central Italy, *J Struct Geol*, 26, 339-376, 2004.

963 Robinson, R., Nicol, A., Walsh, J. J., and Villamor, P.: Features of earthquake
964 occurrence in a complex normal fault network: Results from a synthetic
965 seismicity model of the Taupo Rift, New Zealand, *J Geophys Res-Sol Ea*, 114,
966 2009.

967 Rovida, A., Locati, M., Camassi, R., Lolli, B., and Gasperini P.: CPTI15, the 2015
968 version of the Parametric Catalogue of Italian Earthquakes. Istituto Nazionale
969 di Geofisica e Vulcanologia. doi:<http://doi.org/10.6092/INGV.IT-CPTI15>, 2016.

970 Scotti, O., Clement, C., and Baumont, D.: Seismic hazard for design and verification
971 of nuclear installations in France: regulatory context, debated issues and
972 ongoing developments, *B Geofis Teor Appl*, 55, 135-148, 2014.

973 Stein, R. S., King, G. C. P., and Lin, J.: Stress Triggering of the 1994 M=6.7
974 Northridge, California, Earthquake by Its Predecessors, *Science*, 265, 1432-
975 1435, 1994.

976 Stirling, M., McVerry, G., Gerstenberger, M., Litchfield, N., Van Dissen, R.,
977 Berryman, K., Barnes, P., Wallace, L., Villamor, P., Langridge, R., Lamarche,
978 G., Nodder, S., Reyners, M., Bradley, B., Rhoades, D., Smith, W., Nicol, A.,
979 Pettinga, J., Clark, K., and Jacobs, K.: National Seismic Hazard Model for
980 New Zealand: 2010 Update, *B Seismol Soc Am*, 102, 1514-1542, 2012.

981 Stock, C. and Smith, E. G. C.: Adaptive kernel estimation and continuous probability
982 representation of historical earthquake catalogs, *B Seismol Soc Am*, 92, 904-
983 912, 2002a.

984 Stock, C. and Smith, E. G. C.: Comparison of seismicity models generated by
985 different kernel estimations, *B Seismol Soc Am*, 92, 913-922, 2002b.

986 Stucchi, M., Meletti, C., Montaldo, V., Crowley, H., Calvi, G. M., and Boschi, E.:
987 Seismic Hazard Assessment (2003-2009) for the Italian Building Code, *B*
988 *Seismol Soc Am*, 101, 1885-1911, 2011.

989 Verdecchia, A. and Carena, S.: Coulomb stress evolution in a diffuse plate boundary:
990 1400 years of earthquakes in eastern California and western Nevada, USA,
991 *Tectonics*, 35, 1793-1811, 2016.

992 Visini, F. and Pace, B.: Insights on a Key Parameter of Earthquake Forecasting, the
993 Coefficient of Variation of the Recurrence Time, Using a Simple Earthquake
994 Simulator, *Seismol Res Lett*, 85, 703-713, 2014.

995 Weichert, D. H: Estimation of the earthquake recurrence parameters for unequal
996 observation periods for different magnitudes, *Bulletin of the Seismological*
997 *Society of America*, 70, 1337-1346, 1980.

998 Wells, D. L. and Coppersmith, K. J.: New Empirical Relationships among Magnitude,
999 Rupture Length, Rupture Width, Rupture Area, and Surface Displacement, *B*
1000 *Seismol Soc Am*, 84, 974-1002, 1994.

1001 Werner, M. J., Helmstetter, A., Jackson, D. D., Kagan, Y. Y., and Wiemer, S.:
1002 Adaptively smoothed seismicity earthquake forecasts for Italy, *Ann Geophys-*
1003 *Italy*, 53, 107-116, 2010.

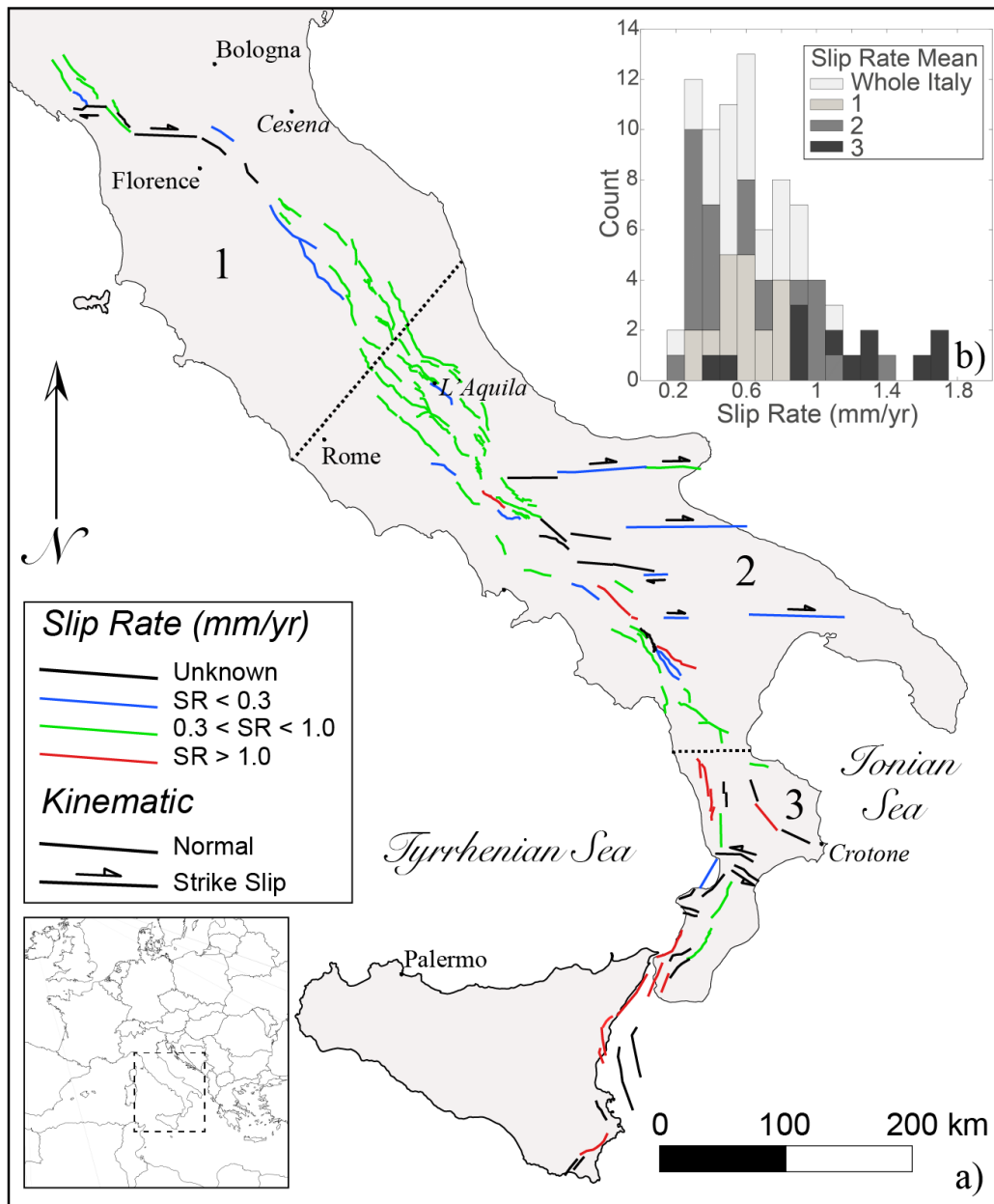
1004 Woessner, J., Laurentiu, D., Giardini, D., Crowley, H., Cotton, F., Grunthal, G.,
1005 Valensise, G., Arvidsson, R., Basili, R., Demircioglu, M. B., Hiemer, S.,
1006 Meletti, C., Musson, R. W., Rovida, A. N., Sesetyan, K., Stucchi, M., and
1007 Consortium, S.: The 2013 European Seismic Hazard Model: key components
1008 and results, *B Earthq Eng*, 13, 3553-3596, 2015.

1009 Youngs, R. R. and Coppersmith, K. J.: Implications of Fault Slip Rates and
1010 Earthquake Recurrence Models to Probabilistic Seismic Hazard Estimates, *B*
1011 *Seismol Soc Am*, 75, 939-964, 1985.

1012 Zechar, J. D. and Jordan, T. H.: Simple smoothed seismicity earthquake forecasts
1013 for Italy, *Ann Geophys-Italy*, 53, 99-105, 2010.

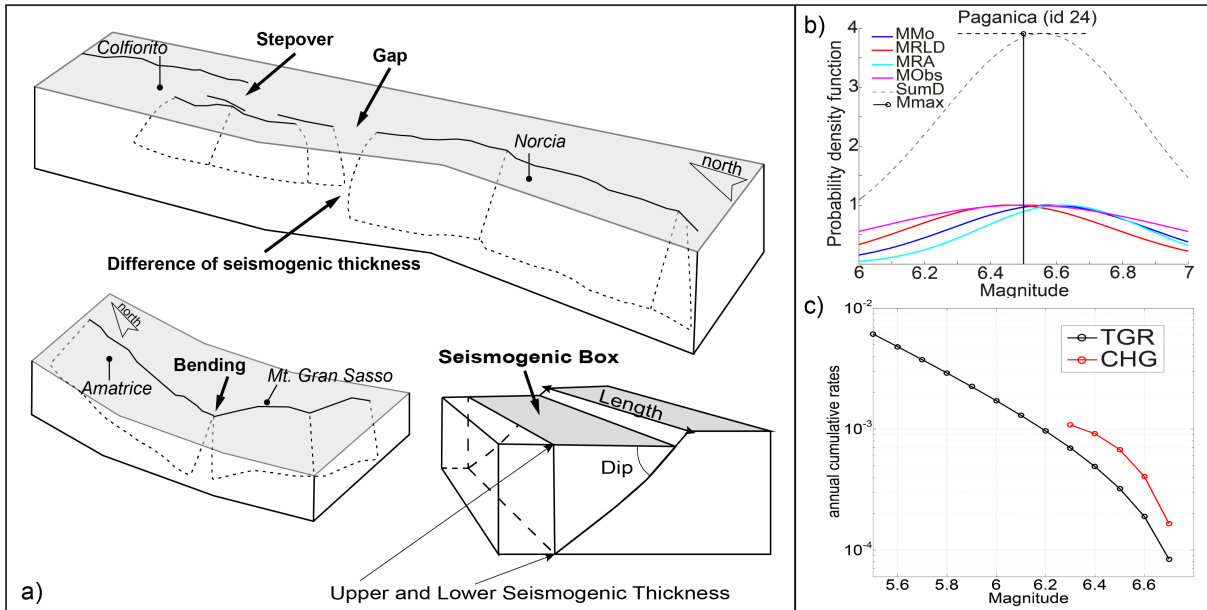
1014 Zhao, J. X., Zhang, J., Asano, A., Ohno, Y., Oouchi, T., Takahashi, T., Ogawa, H.,
1015 Irikura, K., Thio, H. K., Somerville, P. G., Fukushima, Y., and Fukushima, Y.:
1016 Attenuation relations of strong ground motion in Japan using site classification
1017 based on predominant period, *B Seismol Soc Am*, 96, 898-913, 2006.

1018



1019

1020 Fig. 1 a) Map of normal and strike-slip active faults used in this study. The colour
 1021 scale indicates the slip rate. b) Histogram of the slip rate distribution in the entire
 1022 study area and in three subsectors. The numbers 1, 2 and 3 represent the Northern
 1023 Apennines, Central-Southern Apennines and Calabria-Sicilian coast regions,
 1024 respectively. The dotted black lines are the boundaries of the regions.



1025

1026

1027

1028

1029

1030

1031

1032

1033

1034

1035

1036

1037

1038

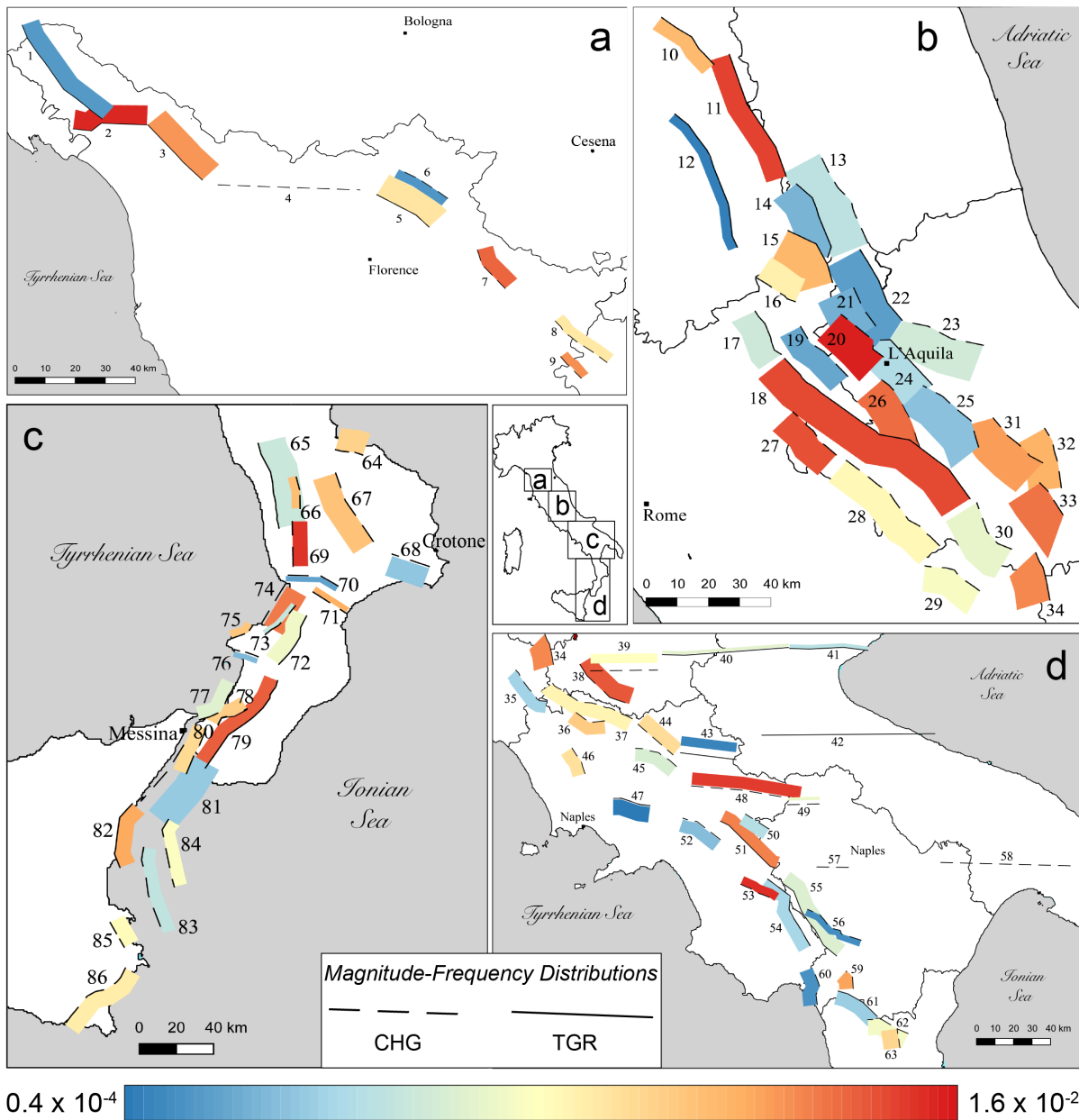
1039

1040

1041

1042

Fig. 2 a) Conceptual model of active faults and segmentation rules adopted to define a fault source and its planar projection, forming a seismogenic box [modified from Boncio et al., 2004]. b) Example of FiSH code output (see Pace et al., 2016 for details) for the Paganica fault source showing the magnitude estimates from empirical relationships and observations, both of which are affected by uncertainties. In this example, four magnitudes are estimated: M_{Mo} (blue line) is from the standard formula (IASPEI, 2005); M_{RLD} (red line) and M_{RA} (cyan line) correspond to estimates based on the maximum subsurface fault length and maximum rupture area from the empirical relationships of Wells and Coppersmith (1994) for length and area, respectively; and M_{Obs} (magenta line) is the largest observed moment magnitude. The black dashed line represents the summed probability density curve (SumD), the vertical black line represents the central value of the Gaussian fit of the summed probability density curve (M_{max}), and the horizontal black dashed line represents its standard deviation (σ M_{max}). The input values that were used to obtain this output are provided in Table 1. c) Comparison of the magnitude–frequency distributions of the Paganica source, which were obtained using the CHG model (red line) and the TGR model (black line).



0.4 x 10⁻⁴ 1.6 x 10⁻²

Activity Rates (#eq $M \geq 5.5$ in a year)

1043

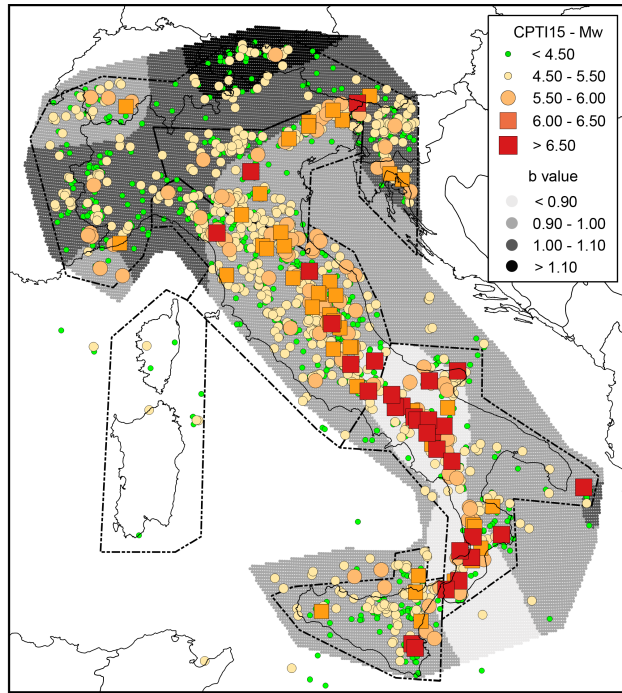
1044

1045

1046

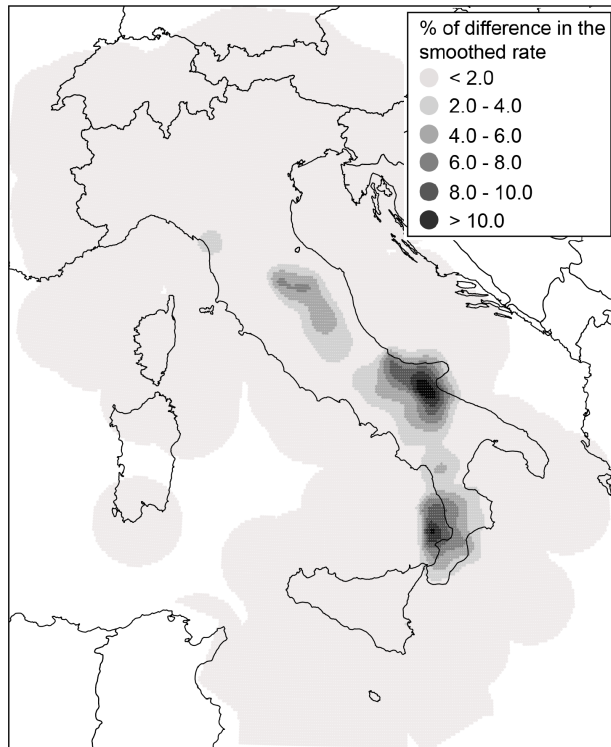
1047

Fig. 3 Maps showing the fault source inputs as seismicogenic boxes (see Fig. 2a). The colour scale indicates the activity rate. Solid and dashed lines (corresponding to the uppermost edge of the fault) are used to highlight our choice between the two end-members of the MFD model adopted in the so-called *Mixed* model.



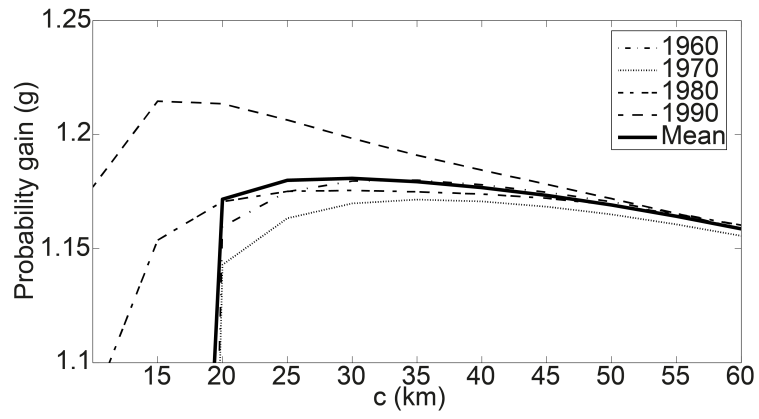
1048

1049 Fig. 4 Historical earthquakes from the most recent version of the historical
 1050 parametric Italian catalogue (CPTI15, Rovida et al., 2016), the spatial variations in b-
 1051 values and the polygons defining the five macroseismic areas used to assess the
 1052 magnitude completeness intervals (Stucchi et al, 2011).



1053

1054 Fig. 5 Differences in percentages between the two smoothed rates computed with
 1055 eq. (2) using the complete catalogue and the modified catalogue without events
 1056 associated with known active faults (*TGR* model)



1057

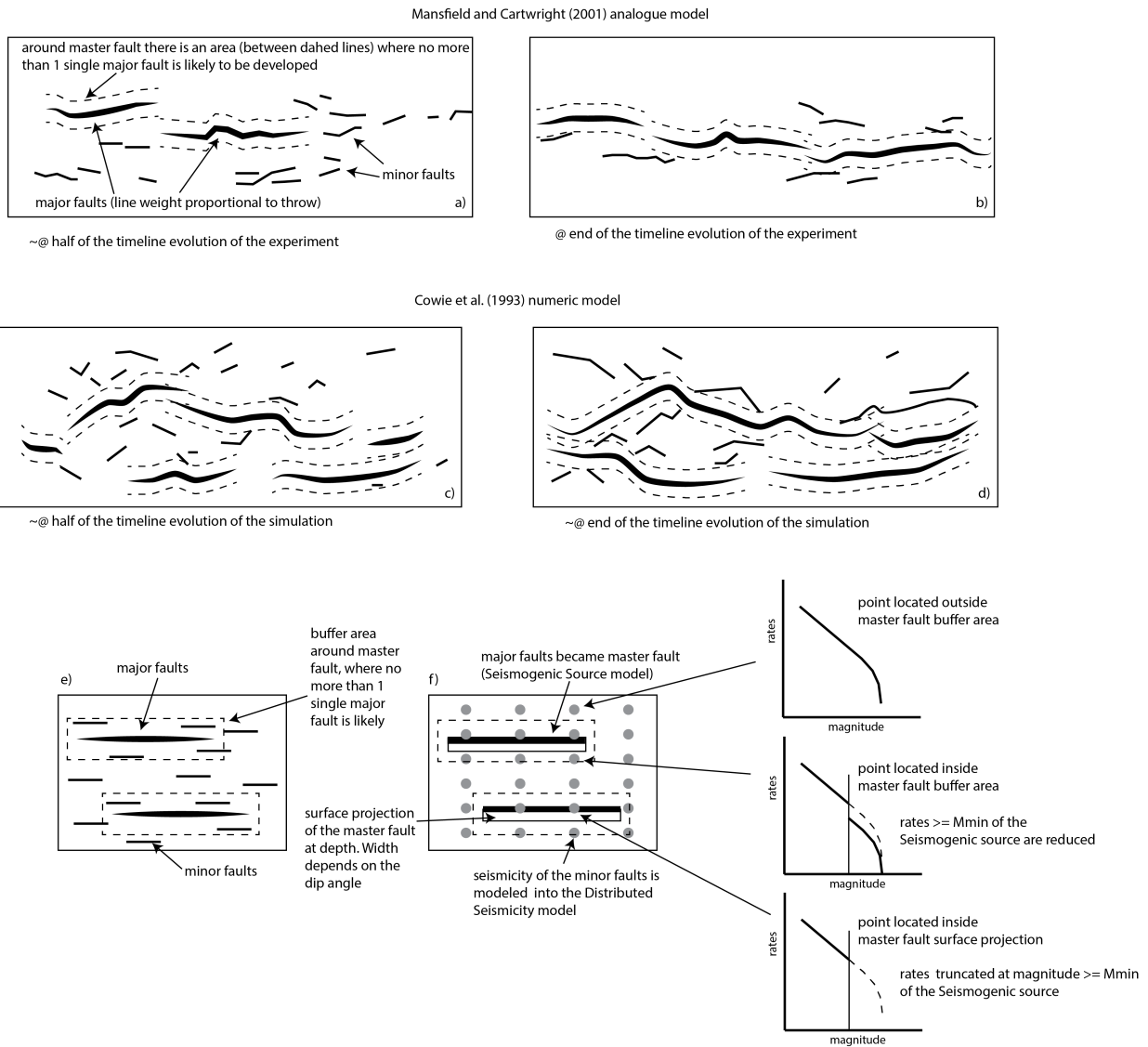
1058 Fig. 6 Probability gain per earthquake (see eq. 3) versus correlation distance c , used
 1059 to determine the best radius for use in the smoothed seismicity approach (eq. 2)

1060

1061

1062

1063



1064

1065

1066

1067

1068

1069

1070

1071

1072

1073

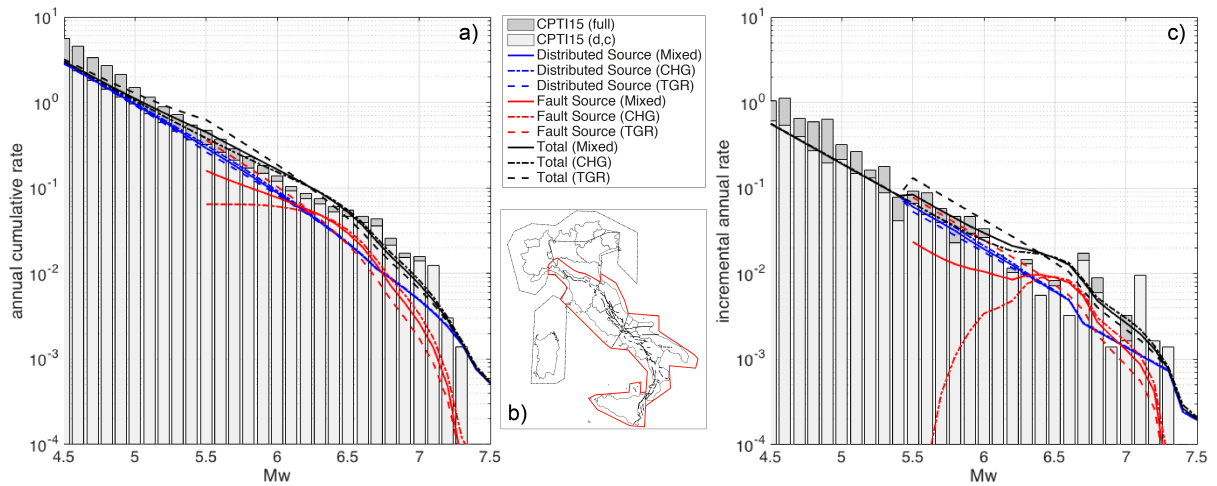
1074

1075

1076

1077

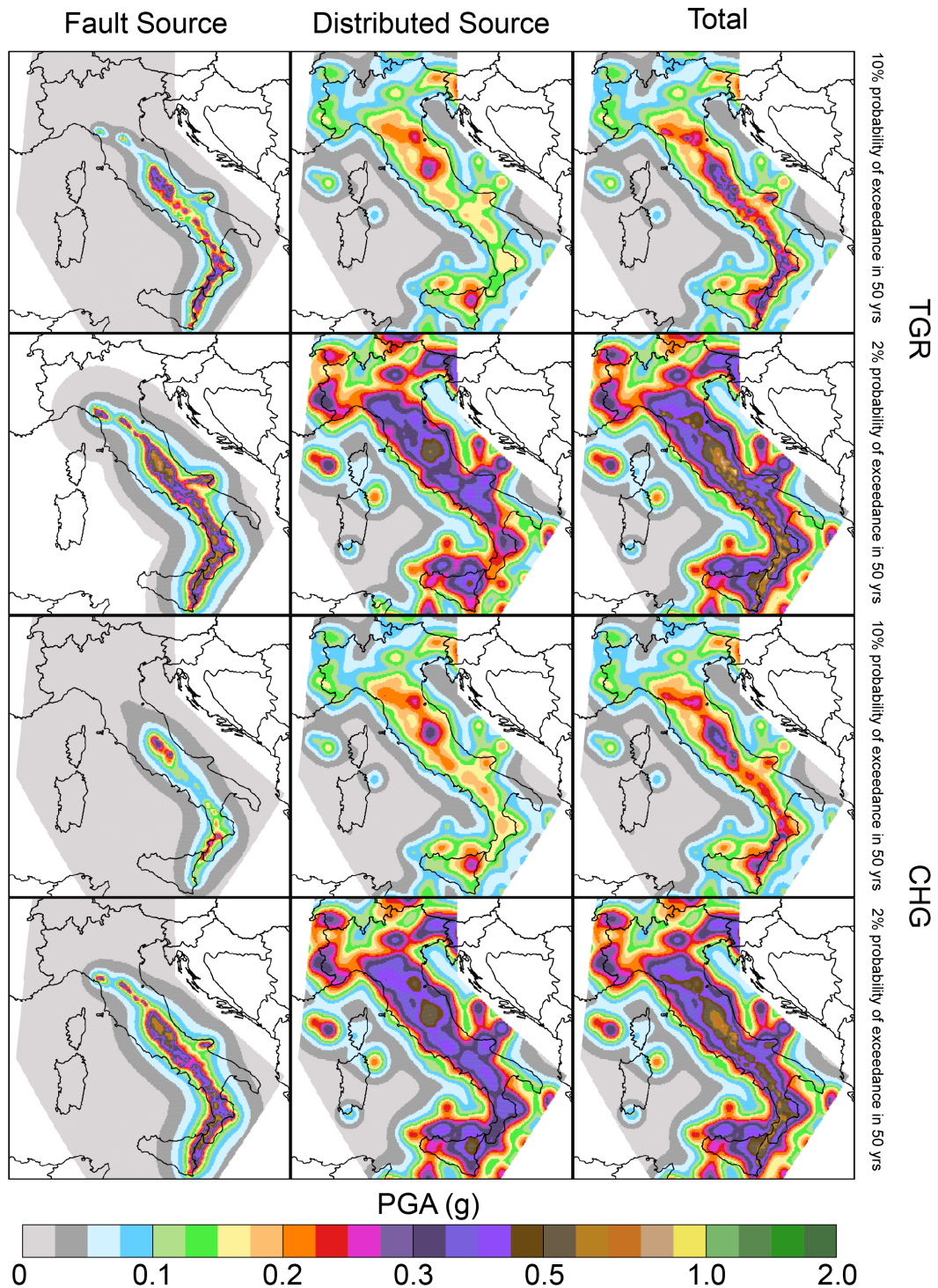
Fig. 7 Fault system evolution and its implications for our model. a) and b) Diagrams from the Mansfield and Cartwright (2001) analogue experiment in two different stages: the approximate midpoint of the sequence and the end of the sequence. Areas exist around master faults where no more than a single major fault is likely to develop. c) and d) Diagrams from numerical modelling conducted by Cowie et al. (1993) in two different stages. This experiment shows the similar evolutionary features of major and minor faults. e) and f) Application of the analogue and numerical modelling of fault system evolution to the fault source input proposed in this paper. A buffer area is drawn around each fault source, where it is unlikely for other major faults to develop, accounting for the length and slip rate of the fault source. This buffer area is useful for reducing or truncating the rates of expected distributed seismicity based on the position of a distributed seismicity point with respect to the buffer zone (see the text for details).



1078

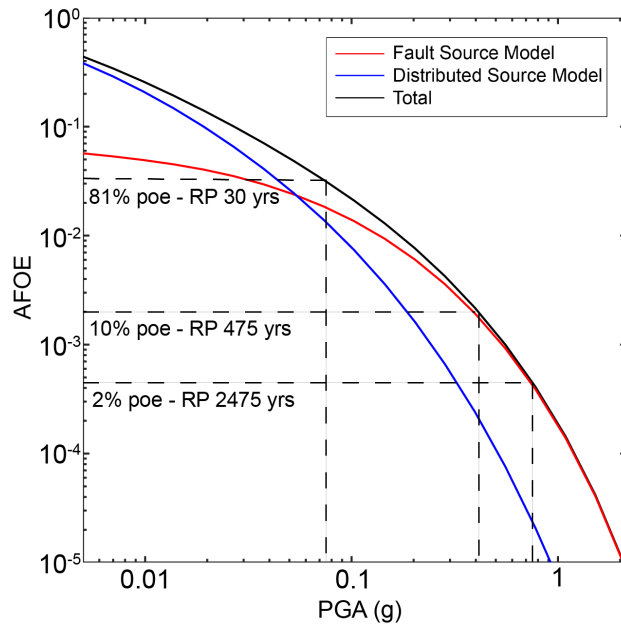
1079 Fig. 8 a) Annual cumulative MFD and c) incremental annual MFD computed for the
 1080 red bounded area in b). The rates have been computed using: (i) the full CPTI15
 1081 catalogue; (ii) the declustered and complete catalogue (CPTI15 (d, c) in the legend)
 1082 obtained using the completeness magnitude thresholds over different periods of time
 1083 given by Stucchi et al. (2011) for five large zones; (iii) the distributed sources; (iv) the
 1084 fault sources; and (v) summing fault and distributed sources (Total).

1085



1086

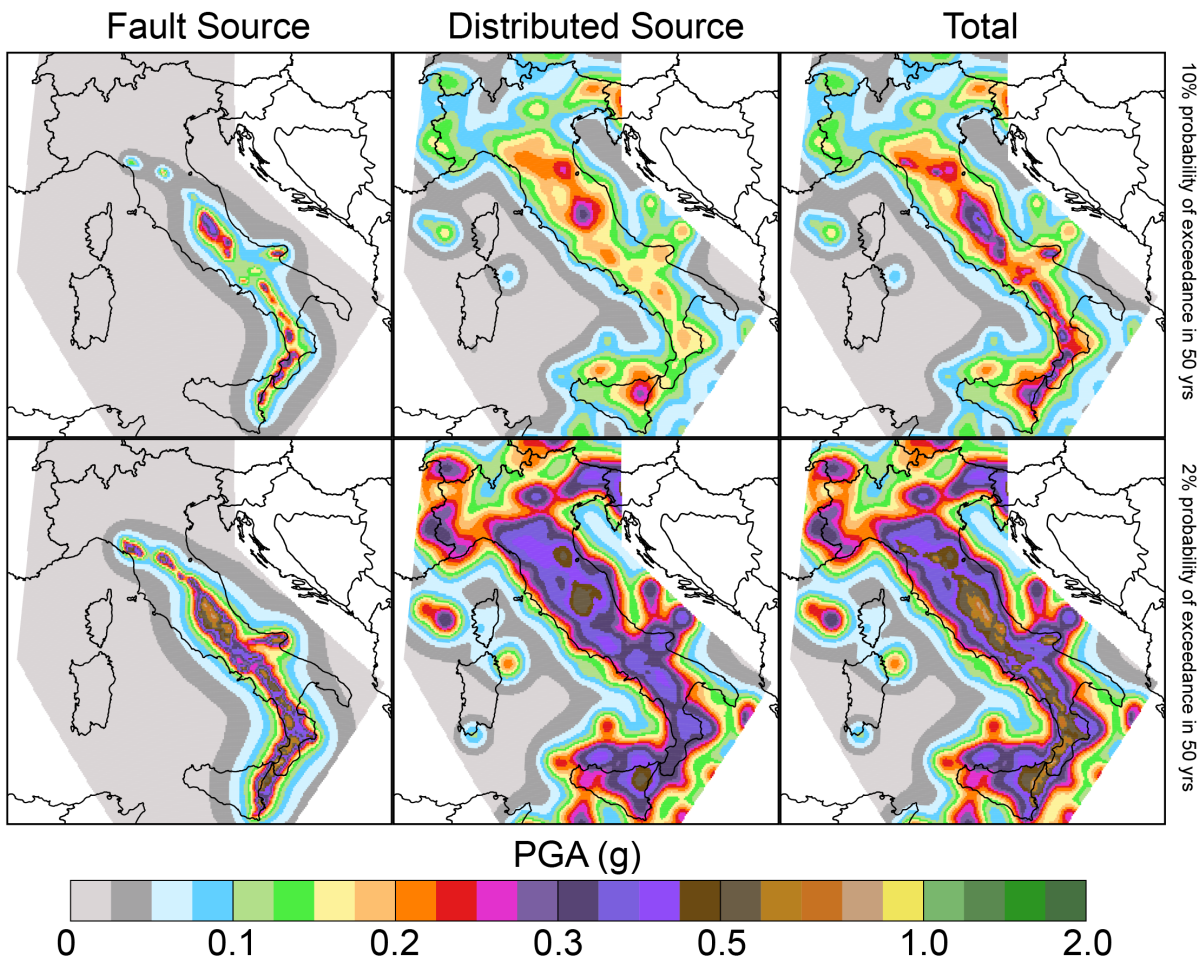
1087 Fig. 9 Seismic hazard maps for the *TGR* and *CHG* models expressed in terms of
 1088 peak ground acceleration (PGA) and computed for a latitude/longitude grid spacing
 1089 of 0.05° . The first and second rows show the fault source, distributed source and
 1090 total maps of the *TGR* model computed for 10% probability of exceedance in 50
 1091 years and 2% probability of exceedance in 50 years, corresponding to return periods
 1092 of 475 and 2475 years, respectively. The third and fourth rows show the same maps
 1093 for the *CHG* model.



1094

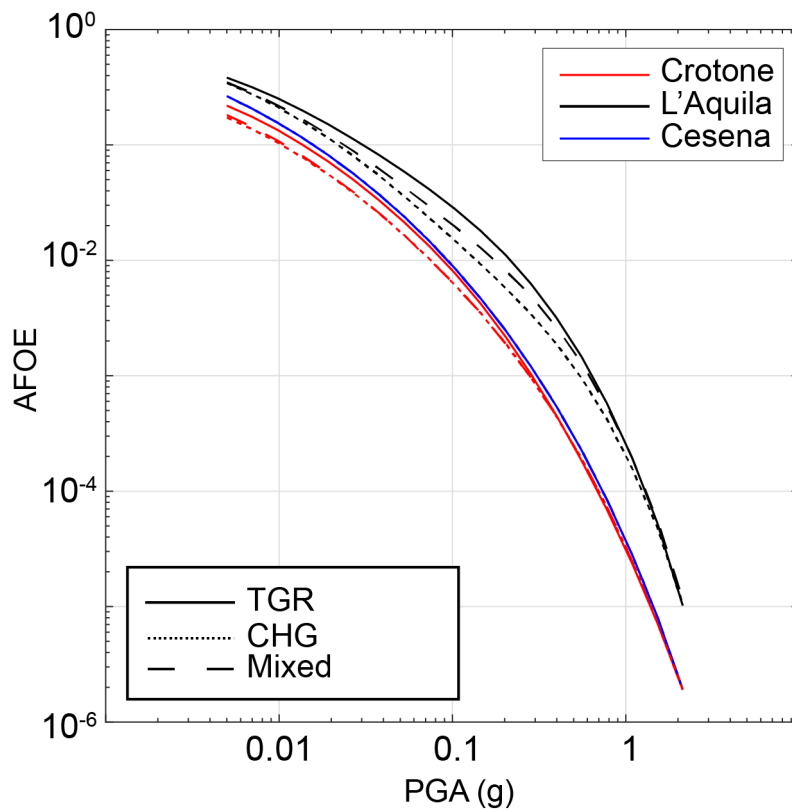
1095 Fig. 10 An example of the contribution to the total seismic hazard level (black line), in
 1096 terms of hazard curves, by the *fault* (red line) and *distributed* (blue line) source inputs
 1097 for one of the 45,602 grid points (L'Aquila, 42.400-13.400). The dashed lines
 1098 represent the 2%, 10% and 81% probabilities of exceedance (poes) in 50 years.

1099



1100
 1101
 1102
 1103
 1104
 1105
 1106
 1107

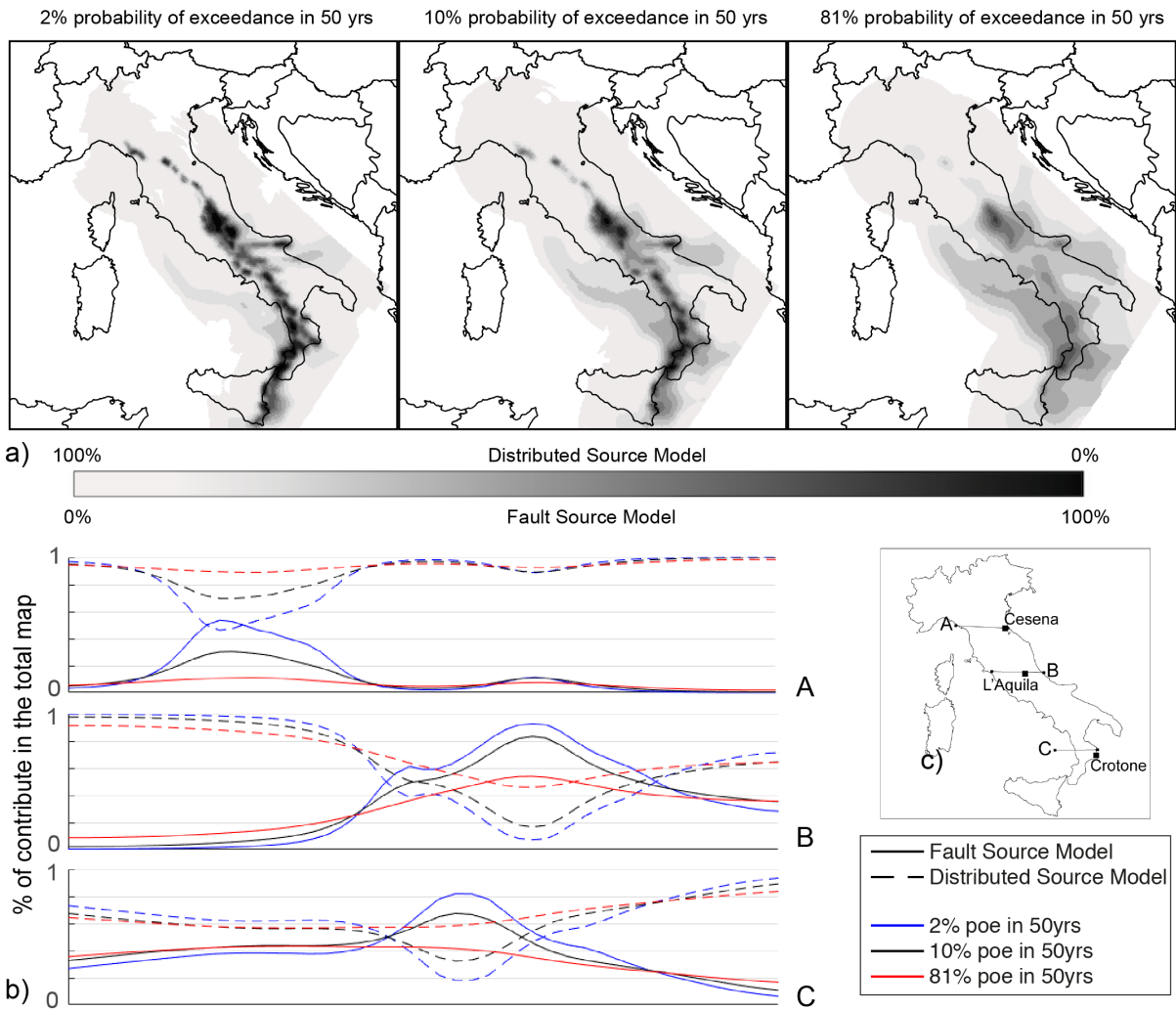
Fig. 11 Seismic hazard maps for the *Mixed* model. The first row shows the fault source, distributed source and total maps computed for 10% probability of exceedance in 50 years, and the second row shows the same maps but computed for 2% probability of exceedance in 50 years, corresponding to return periods of 475 and 2475 years, respectively. The results are expressed in terms of peak ground acceleration (PGA).



1108

1109 Fig. 12 *CHG* (dotted line), *TGR* (solid line) and *Mixed* model (dashed line) hazard
 1110 curves for three sites (see Fig. 13 for the location): Cesena (red line), L'Aquila (black
 1111 line) and Crotone (blue line)

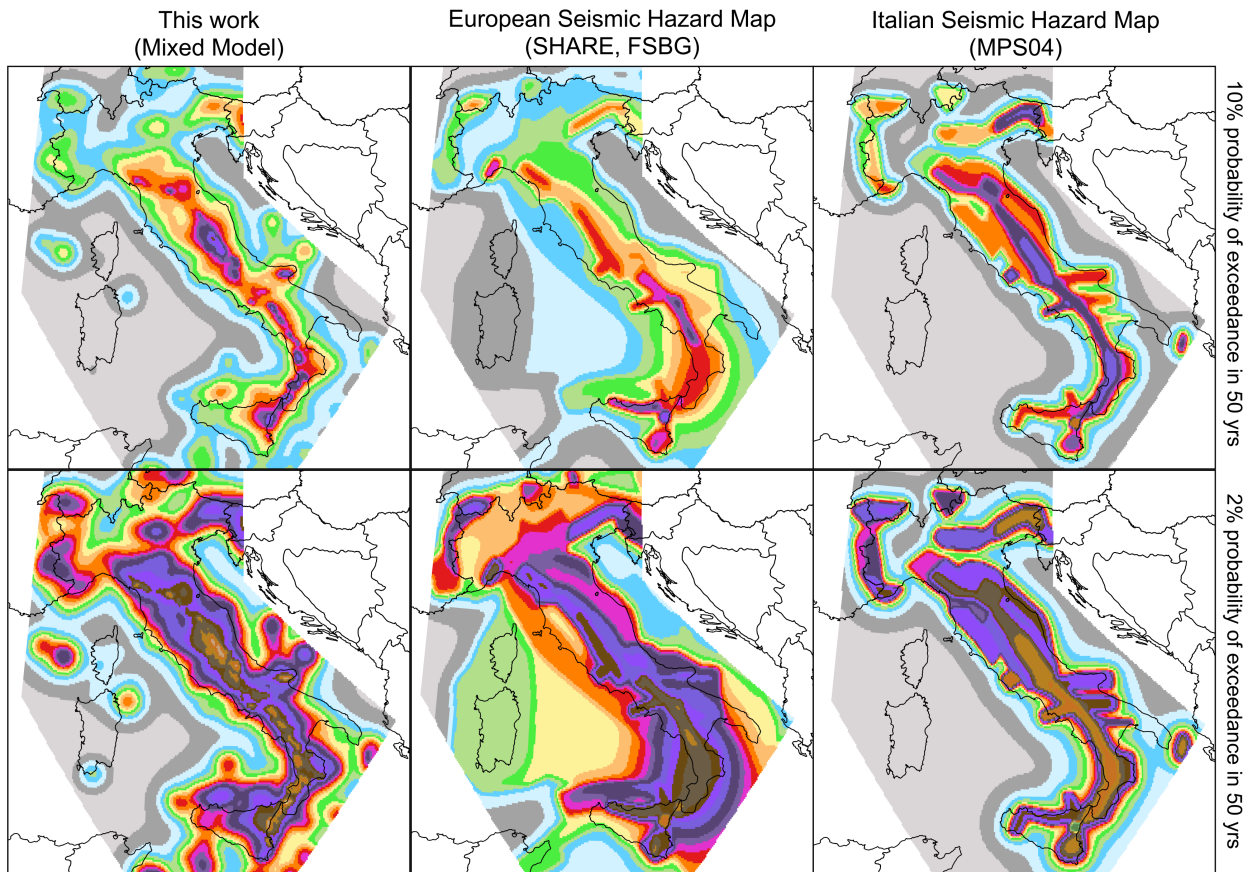
1112



1113

1114

1115 Fig. 13 a) Contribution maps of the Mixed *fault* and *distributed* source inputs to the
 1116 total hazard level for three probabilities of exceedance: 2%, 10% and 81%,
 1117 corresponding to return periods of 2475, 475 and 30 years, respectively. b)
 1118 Contributions of the Mixed *fault* (solid line) and *distributed* (dashed line) source
 1119 inputs along three profiles (A, B and C in Fig. 13c) for three probabilities of
 1120 exceedance: 2% (blue line), 10% (black line) and 81% (red line).



1121

1122 Fig. 14 Seismic hazard maps expressed in terms of Peak Ground Acceleration
 1123 (PGA) and computed for a latitude/longitude grid spacing of 0.05° based on rock site
 1124 conditions. The figure shows a comparison of our model (*Mixed* model, on the left),
 1125 the ESHM13 model (FSBG logic tree branch, in the middle) and the current Italian
 1126 national seismic hazard map (MPS04, on the right). The same combination of
 1127 GMPEs (Akkar et al. 2013, Chiou et al., 2008, Faccioli et al., 2010 and Zhao et al.,
 1128 2006 and Bindi et al. 2014), were used for all models to obtain and compare the
 1129 maps.

1130

1131

1132

1133

1134

ID	Fault Sources	L (km)	Dip (°)	Upper (km)	Lower (km)	SR _{min} (mm/yr)	SR _{max} (mm/yr)
1	Lunigiana	43.8	40	0	5	0.28	0.7
2	North Apuane Transfer	25.5	45	0	7	0.33	0.83
3	Garfagnana	26.9	30	0	4.5	0.35	0.57
4	Garfagnana Transfer	47.1	90	2	7	0.33	0.83
5	Mugello	21.0	40	0	7	0.33	0.83
6	Ronta	19.3	65	0	7	0.17	0.5
7	Poppi	17.1	40	0	4.5	0.33	0.83
8	Città di Castello	22.9	40	0	3	0.25	1.2
9	M.S.M. Tiberina	10.5	40	0	2.5	0.25	0.75
10	Gubbio	23.6	50	0	6	0.4	1.2
11	Colfiorito System	45.9	50	0	8	0.25	0.9
12	Umbra Valley	51.1	55	0	4.5	0.4	1.2
13	Vettore-Bove	35.4	50	0	15	0.2	1.05
14	Nottoria-Preci	29.0	50	0	12	0.2	1
15	Cascia-Cittareale	24.3	50	0	13.5	0.2	1
16	Leonessa	14.9	55	0	12	0.1	0.7
17	Rieti	17.6	50	0	10	0.25	0.6
18	Fucino	82.3	50	0	13	0.3	1.6
19	Sella di Corno	23.1	60	0	13	0.35	0.7
20	Pizzoli-Pettino	21.3	50	0	14	0.3	1
21	Monte Reale	15.1	50	0	14	0.25	0.9
22	Gorzano	28.1	50	0	15	0.2	1
23	Gran Sasso	28.4	50	0	15	0.35	1.2
24	Paganica	23.7	50	0	14	0.4	0.9
25	Middle Aternum Valley	29.1	50	0	14	0.15	0.45
26	Campo Felice-Ovindoli	26.2	50	0	13	0.2	1.6
27	Carsoli	20.5	50	0	11	0.35	0.6
28	Liri	42.5	50	0	11	0.3	1.26
29	Sora	20.4	50	0	11	0.15	0.45
30	Marsicano	20.0	50	0	13	0.25	1.2
31	Sulmona	22.6	50	0	15	0.6	1.35
32	Maiella	21.4	55	0	15	0.7	1.6
33	Aremogna C.Miglia	13.1	50	0	15	0.1	0.6
34	Barrea	17.1	55	0	13	0.2	1
35	Cassino	24.6	60	0	11	0.25	0.5
36	Ailano-Piedimonte	17.6	60	0	12	0.15	0.35
37	Matese	48.3	60	0	13	0.2	1.9
38	Bojano	35.5	55	0	13	0.2	0.9
39	Frosolone	36.1	70	11	25	0.35	0.93
40	Ripabottoni-San Severo	68.3	85	6	25	0.1	0.5
41	Mattinata	42.3	85	0	25	0.7	1
42	Castelluccio dei Sauri	93.2	90	11	22	0.1	0.5
43	Ariano Irpino	30.1	70	11	25	0.35	0.93
44	Tammaro	25.0	60	0	13	0.35	0.93
45	Benevento	25.0	55	0	10	0.35	0.93
46	Volturno	15.7	60	1	13	0.23	0.57
47	Avella	20.5	55	1	13	0.2	0.7
48	Ufita-Bisaccia	59.0	64	1.5	15	0.35	0.93

49	Melfi	17.2	80	12	22	0.1	0.5
50	Irpinia Antithetic	15.0	60	0	11	0.2	0.53
51	Irpinia	39.7	65	0	14	0.3	2.5
52	Vulturara	23.7	60	1	13	0.2	0.35
53	Alburni	20.4	60	0	8	0.35	0.7
54	Caggiano-Diano Valley	46.0	60	0	12	0.35	1.15
55	Pergola-Maddalena	50.6	60	0	12	0.20	0.93
56	Agri	34.9	50	5	15	0.8	1.3
57	Potenza	17.8	90	15	21	0.1	0.5
58	Palagianello	73.3	90	13	22	0.1	0.5
59	Monte Alpi	10.9	60	0	13	0.35	0.9
60	Maratea	21.6	60	0	13	0.46	0.7
61	Mercure	25.8	60	0	13	0.2	0.6
62	Pollino	23.8	60	0	15	0.22	0.58
63	Castrovillari	10.3	60	0	15	0.2	1.15
64	Rossano	14.9	60	0	22	0.5	0.6
65	Crati West	49.7	45	0	15	0.84	1.4
66	Crati East	18.4	60	0	8	0.75	1.45
67	Lakes	43.6	60	0	22	0.75	1.45
68	Fuscalto	21.1	60	2	22	0.75	1.45
69	Piano Lago-Decollatura	25.0	60	1	15	0.23	0.57
70	Catanzaro North	29.5	80	3	20	0.75	1.45
71	Catanzaro South	21.3	80	3	20	0.75	1.45
72	Serre	31.6	60	0	15	0.7	1.15
73	Vibo	23.0	80	0	15	0.75	1.45
74	Sant'Eufemia Gulf	24.8	40	1	11	0.11	0.3
75	Capo Vaticano	13.7	60	0	8	0.75	1.45
76	Coccorino	13.3	70	3	11	0.75	1.45
77	Scilla	29.7	60	0	13	0.8	1.5
78	Sant'Eufemia	19.2	60	0	13	0.75	1.45
79	Cittanova-Armo	63.8	60	0	13	0.45	1.45
80	Reggio Calabria	27.2	60	0	13	0.7	2
81	Taormina	38.7	30	3	13	0.9	2.6
82	Acireale	39.4	60	0	15	1.15	2.3
83	Western Ionian	50.1	65	0	15	0.75	1.45
84	Eastern Ionian	39.3	65	0	15	0.75	1.45
85	Climiti	15.7	60	0	15	0.75	1.45
86	Avola	46.9	60	0	16	0.8	1.6

1136

1137 Table 1 Geometric Parameters of the Fault Sources. L, along-strike length; Dip,
1138 inclination angle of the fault plane; Upper and Lower, the thickness bounds of the
1139 local seismogenic layer; SRmin and SRmax, the minimum and maximum slip rates
1140 assigned to the sources using the references available (see the supplemental files);
1141 and *ID*, the fault number identifier.

1142

ID	Fault Sources	Historical Earthquakes				Instrumental Earthquakes		
		yyyy/mm/dd	I_{Max}	I_0	M_w	sD	yyyy/mm/dd	M_w
1	Lunigiana	1481/05/07	VIII	VIII	5.6	0.4		
		1834/02/14	IX	IX	6.0	0.1		
2	North Apuane Transfer	1837/04/11	X	IX	5.9	0.1		
3	Garfagnana	1740/03/06	VIII	VIII	5.6	0.2		
		1920/09/07	X	X	6.5	0.1		
4	Garfagnana Transfer							
5	Mugello	1542/06/13	IX	IX	6.0	0.2		
		1919/06/29	X	X	6.4	0.1		
6	Ronta							
7	Poppi							
8	Città di Castello	1269			5.7			
		1389/10/18	IX	IX	6	0.5		
		1458/04/26	VIII-IX	VIII-IX	5.8	0.5		
		1789/09/30	IX	IX	5.9	0.1		
9	M.S.M. Tiberina	1352/12/25	IX	IX	6.3	0.2		
		1917/04/26	IX-X	IX-X	6.0	0.1		
10	Gubbio						1984/04/29	5.6
11	Colfiorito System	1279/04/30	X	IX	6.2	0.2	1997/09/26	5.7
		1747/04/17	IX	IX	6.1	0.1	1997/09/26	6
		1751/07/27	X	X	6.4	0.1		
12	Umbra Valley	1277		VIII	5.6	0.5		
		1832/01/13	X	X	6.4	0.1		
		1854/02/12	VIII	VIII	5.6	0.3		
13	Vettore-Bove						2016/10/30	6.5
14	Nottoria-Preci	1328/12/01	X	X	6.5	0.3	1979/09/19	5.8
		1703/01/14	XI	XI	6.9	0.1		
		1719/06/27	VIII	VIII	5.6	0.3		
		1730/05/12	IX	IX	6.0	0.1		
		1859/08/22	VIII-IX	VIII-IX	5.7	0.3		
		1879/02/23	VIII	VIII	5.6	0.3		
15	Cascia-Cittareale	1599/11/06	IX	IX	6.1	0.2		
		1916/11/16	VIII	VIII	5.5	0.1		
16	Leonessa							
17	Rieti	1298/12/01	X	IX-X	6.3	0.5		
		1785/10/09	VIII-IX	VIII-IX	5.8	0.2		
18	Fucino	1349/09/09	IX	IX	6.3	0.1		
		1904/02/24	IX	VIII-IX	5.7	0.1		
		1915/01/13	XI	XI	7	0.1		
19	Sella di Corno							
20	Pizzoli-Pettino	1703/02/02	X	X	6.7	0.1		
21	Monte Reale							
22	Gorzano	1639/10/07	X	IX-X	6.2	0.2		
		1646/04/28	IX	IX	5.9	0.4		
23	Gran Sasso							
24	Paganica	1315/12/03	VIII	VIII	5.6	0.5	2009/06/04	6.3
		1461/11/27	X	X	6.5	0.5		
25	Middle Aternum Valley							
26	Campo Felice-Ovindoli							
27	Carsoli							
28	Liri							
29	Sora	1654/07/24	X	IX-X	6.3	0.2		
30	Marsicano							
31	Sulmona							
32	Maiella							
33	Aremogna C.Miglia							
34	Barrea						1984/05/07	5.9
35	Cassino							
36	Ailano-Piedimonte							
37	Matese	1349/09/09	X-XI	X	6.8	0.2		

38	Bojano	1805/07/26	X	X	6.7	0.1		
39	Frosolone	1456/12/05	XI	XI	7	0.1		
40	Ripabottoni-San Severo	1627/07/30	X	X	6.7	0.1	2002/10/31	5.7
		1647/05/05	VII-VIII	VII-VIII	5.7	0.4		
		1657/01/29	IX-X	VIII-IX	6.0	0.2		
41	Mattinata	1875/12/06	VIII	VIII	5.9	0.1		
		1889/12/08	VII	VII	5.5	0.1		
		1948/08/18	VII-VIII	VII-VIII	5.6	0.1		
42	Castelluccio dei Sauri	1361/07/17	X	IX	6	0.5		
		1560/05/11	VIII	VIII	5.7	0.5		
		1731/03/20	IX	IX	6.3	0.1		
43	Ariano Irpino	1456/12/05			6.9	0.1		
		1962/08/21	IX	IX	6.2	0.1		
44	Tammaro	1688/06/05	XI	XI	7	0.1		
45	Benevento							
46	Volturno							
47	Avella	1499/12/05	VIII	VIII	5.6	0.5		
48	Ufita-Bisaccia	1732/11/29	X-XI	X-XI	6.8	0.1		
		1930/07/23	X	X	6.7	0.1		
49	Melfi	1851/08/14	X	X	6.5	0.1		
50	Irpinia Antithetic							
51	Irpinia	1466/01/15	VIII-IX	VIII-IX	6.0	0.2	1980/11/23	6.8
		1692/03/04	VIII	VIII	5.9	0.4		
		1694/09/08	X	X	6.7	0.1		
		1853/04/09	IX	VIII	5.6	0.2		
52	Volturara							
53	Alburni							
54	Caggiano-Diano Valley	1561/07/31	IX-X	X	6.3	0.1		
55	Pergola-Maddalena	1857/12/16			6.5			
		1857/12/16			6.3			
56	Agri							
57	Potenza	1273/12/18	VIII-IX	VIII-IX	5.8	0.5	1990/05/05	5.8
58	Palagianello							
59	Monte Alpi							
60	Maratea							
61	Mercure	1708/01/26	VIII-IX	VIII	5.6	0.6	1998/09/09	5.5
62	Pollino							
63	Castrovillari							
64	Rossano	1836/04/25	X	IX	6.2	0.2		

65	Crati West	1184/05/24	IX	IX	6.8	0.3
		1870/10/04	X	IX-X	6.2	0.1
		1886/03/06	VII-VIII	VII-VIII	5.6	0.3
66	Crati East	1767/07/14	VIII-IX	VIII-IX	5.9	0.2
		1835/10/12	X	IX	5.9	0.3
67	Lakes	1638/06/08	X	X	6.8	0.1
68	Fuscalto	1832/03/08	X	X	6.6	0.1
69	Piano Lago-Decollatura					
70	Catanzaro North	1638/03/27			6.6	
71	Catanzaro South	1626/04/04	X	IX	6.1	0.4
72	Serre	1659/11/05	X	X	6.6	0.1
		1743/12/07	IX-X	VIII-IX	5.9	0.2
		1783/02/07	X-XI	X-XI	6.7	0.1
		1791/10/13	IX	IX	6.1	0.1
73	Vibo					
74	Sant'Eufemia Gulf	1905/09/08	X-XI	X-XI	7	0.1
75	Capo Vaticano					
76	Coccorino	1928/03/07	VIII	VII-VIII	5.9	0.1
77	Scilla					
78	Sant'Eufemia	1894/11/16	IX	IX	6.1	0.1
79	Cittanova-Armo	1509/02/25	IX	VIII	5.6	0.4
		1783/02/05	XI	XI	7.1	0.1
80	Reggio Calabria					
81	Taormina	1908/12/28	XI	XI	7.1	0.2
82	Acireale	1818/02/20	IX-X	IX-X	6.3	0.1
83	Western Ionian	1693/01/11	XI	XI	7.3	0.1
84	Eastern Ionian					
85	Climiti					
86	Avola					

1143

1144 Table 2 Earthquake-Source Association Adopted for Fault Sources. I_{Max} , maximum
1145 intensity; I_0 , epicentral intensity; M_w , moment magnitude; and sD, standard deviation
1146 of the moment magnitude. For references, see the supplemental files.